Three-dimensional vibrations of cylindrical elastic solids with V-notches and sharp radial cracks

O.G. McGee III[a],*, J.W. Kim[b]

[a] Department of Mechanical Engineering, Howard University, Washington, DC, USA
[b] Department of Architectural Engineering, Semyung University, Jechon, Chungbuk, South Korea

ARTICLE INFO

ABSTRACT

This paper provides free vibration data for cylindrical elastic solids, specifically thick circular plates and cylinders with V-notches and sharp radial cracks, for which no extensive previously published database is known to exist. Bending moment and shear force singularities are known to exist at the sharp reentrant corner of a thick V-notched plate under transverse vibratory motion, and three-dimensional (3-D) normal and transverse shear stresses are known to exist at the sharp reentrant terminus edge of a V-notched cylindrical elastic solid under 3-D free vibration. A theoretical analysis is done in this work utilizing a variational Ritz procedure including these essential singularity effects. The procedure incorporates a complete set of admissible algebraic–trigonometric polynomials in conjunction with an admissible set of "*edge functions*" that explicitly model the 3-D stress singularities which exist along a reentrant terminus edge (i.e., $\alpha > 180°$) of the V-notch. The first set of polynomials guarantees convergence to exact frequencies, as sufficient terms are retained. The second set of edge functions—in addition to representing the corner stress singularities—substantially accelerates the convergence of frequency solutions. This is demonstrated through extensive convergence studies that have been carried out by the investigators. Numerical analysis has been carried out and the results have been given for cylindrical elastic solids with various V-notch angles and depths. The relative depth of the V-notch is defined as $(1-c/a)$, and the notch angle is defined as $(360°-\alpha)$. For a very small notch angle ($1°$ or less), the notch may be regarded as a "sharp radial crack." Accurate (four significant figure) frequencies are presented for a wide spectrum of notch angles ($360°-\alpha$), depths ($1-c/a$), and thickness ratios (a/h for plates and h/a for cylinders). An extended database of frequencies for completely free thick sectorial, semi-circular, and segmented plates and cylinders are also reported herein as interesting special cases. A generalization of the elasticity-based Ritz analysis and findings applicable here is an arbitrarily shaped V-notched cylindrical solid, being a surface traced out by a family of generatrix, which pass through the circumference of an arbitrarily shaped V-notched directrix curve, $r(\theta)$, several of which are described for future investigations and close extensions of this work.

Published by Elsevier Ltd.

---

* Corresponding author.
  E-mail address: ogmcgee@yahoo.com (O.G. McGee III).

1. Introduction

In the literature, one can find on the order of 1000 published references on vibrations of circular cylindrical shells, based upon 2-D shell theory [1]. However, relatively speaking, very little has been done in the associated literature of three-dimensional (3-D) vibrations characteristics of thick circular cylindrical bodies. Understanding such vibration characteristics require a 3-D prediction procedure, which is based upon 3-D theory of elasticity. A 3-D analysis places none of the kinematic constraints of the 2-D theories. Effective solutions to the 3-D dynamic problems of elastic bodies are very difficult to obtain and, as a result, only a limited number of papers dealing with the free vibrations of thick cylindrical elastic bodies have appeared.

Pochhamer [2] and Chree [3] offered the earliest known studies of the vibration of infinitely long cylindrical solids. Greenspon [4], Gazis [5] and Armenakas [6] extended the early Pochhamer–Chree fundamental work in examining the vibration of infinitely long traction-free hollow cylindrical bodies using 3-D theory of elasticity. Pickett [7] provided some early free vibration solutions for solid cylindrical bodies modeled as circular disks. McNiven and Perry [8] and McNevin et al. [9] developed a three-mode theory for axisymmetric vibrations of elastic bodies modeled as rods and hollow cylinders. Various approximate numerical procedures including finite differences, as well as experimental tests have been employed in examining cylindrical solids idealized as rods and beams [10–16]. Using finite element techniques, the axisymmetric vibrations of cylindrical solids was analyzed by Gladwell and Tahbildar [17], as well as, the vibration of free finite length circular cylindrical solids was predicted by Gladwell and Vijay [18]. Hutchinson [19,20] developed a semi-analytical highly accurate 3-D theory of elasticity solution of the vibrations of finite length elastic solids characteristic of rods and solid cylinders, and Hutchinson and El-Azhari [21] extended the Hutchinson semi-analytical solution to the vibrations of free hollow finite length circular cylindrical bodies. A number of researchers [22–25] have studied the free vibrations of completely free cylindrical bodies, both solid and hollow, by means of either approximate theoretical methods or experimental measurements. Singal and Williams [22] investigated the vibrations of thick hollow cylindrical bodies using an energy method based on the 3-D theory of elasticity. Leissa and So [23,24] and So and Leissa [25] studied the vibrations of free and cantilevered cylindrical solids using simple algebraic polynomial displacement fields in a 3-D elasticity-based Ritz procedure. Liew and Hung [26], Liew et al. [27], and Hung et al. [28] studied the free vibrations of solid and hollow cylindrical bodies having various end conditions using combined orthogonal polynomial-boundary function displacement fields in a similar 3-D elasticity-based Ritz procedure. Convergence of the procedure and parametric investigations were performed for numerous end conditions and cross-sections of hollow cylindrical bodies. Some studies have also been performed on the vibrations of cylindrical bodies that include the classification of natural frequencies or mode shapes, such as the study presented by Wang and Williams [29] using the finite element method. Modified versions of 3-D elasticity-based Ritz approaches using Chebyshev-based admissible displacement fields have been proposed to obtain more accurate and quicker convergence of solutions. For example, Zhou et al. [30] studied 3-D vibrations of solid and hollow cylindrical bodies using such elasticity-based Ritz techniques, adopting a triplicate Chebyshev polynomial series as assumed displacement fields adjusted with admissible boundary functions, and Lee et al. [31] and Ebenezer et al. [32] similarly addressed elasticity-based free and forced vibration solutions of hollow cylindrical bodies.

Furthermore, the scope of previous work done for vibrations of completely free cylindrical elastic solids having V-notches or cracks is very scarce. The V-notches may be generated by various types of machine tools (e.g., milling, grinding and shaping machines), or even by sawing. Cracks are usually created in machine components and civil and aerospace engineering structures and components subjected to cyclic dynamic loading inducing stress fatigue even cracks. The V-notches or cracks not only degrade the structural dynamic performance of civil, aerospace and mechanical components, but also fundamentally cause changes in the natural frequencies and mode shapes of such components.

An eigenfunction expansion technique has been used to analyze the vibrations of classical thin plates with re-entrant corner (boundary-type) singularities (see [33]). In Leissa et al. [33], accurate frequencies and mode shapes were presented for completely free classically thin circular plates with V-notches and sharp radial cracks. The concurrent work of the authors has extended the use of eigenfunction expansion to the vibration of completely free Mindlin sectorial plates. Specifically, the 2-D comparison functions (i.e., Mindlin corner functions), which account for the bending moment and transverse shear force singularities at the vertex of the Mindlin sectorial plates, have been developed using modified Mindlin differential equilibrium equations. The present work extends Leissa et al. [33], McGee and Kim [34], Mindlin [35], and McGee et al. [36] to elastic cylindrical bodies classified as thick circular plates and cylinders having V-notches and sharp radial cracks, for which no previously published vibration characteristics are known to exist. Sih [37], Hartranft and Sih [38], Folias [39], Shaofu et al. [40], Shen [41] and Tandon [42] developed eigenfunctions, which satisfy the 3-D equilibrium equations and stresses for an infinite solid with a crack. In McGee and Kim [34], Sih [37] and Hartranft and Sih [38] procedures have been extended for computational employment in the 3-D vibration analysis of reentrant V-notched cylindrical elastic solids with a finite thickness. A truncated procedure of solving the 3-D equilibrium equations has been used to derive the comparison functions (i.e., 3-D edge functions), which account for tri-axial stress singularities along the terminus reentrant edge of notched elastic solids. In the present analysis, the 3-D dynamical energies of arbitrarily shaped, notched or cracked elastic solids have been maximized using a Ritz procedure with the displacement field approximated by a hybrid trial function of admissible and mathematically complete algebraic–trigonometric polynomials and admissible edge functions that account for the unbounded stresses at the sharp corner/edge of the V-notch.
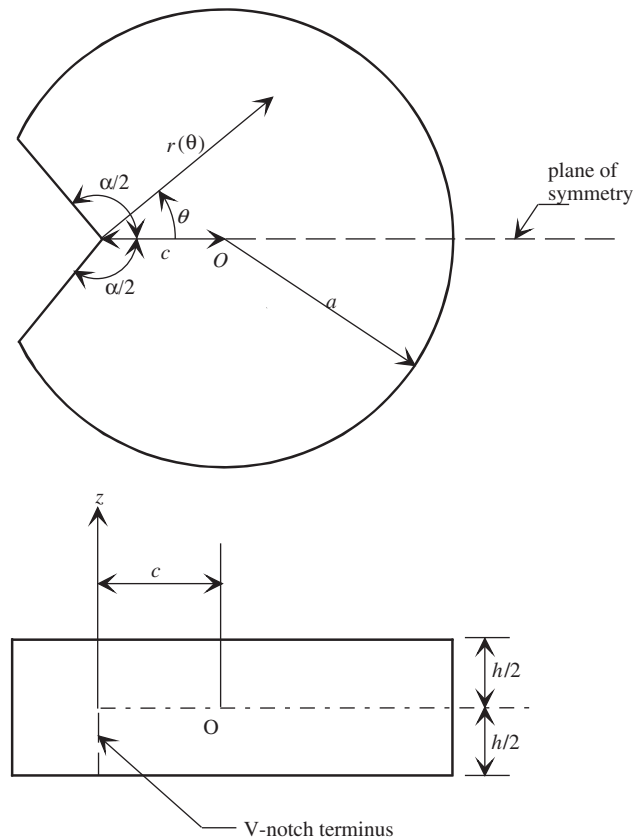
Fig. 1. The 3-D cylindrical solid with a V-notch.

The relative depth of the V-notch of the cylindrical elastic bodies is defined as $(1-c/a)$, and the notch angle is defined as $(360°-\alpha)$ (Fig. 1). For a very small notch angle ($1°$ or less), the notch may be regarded as a radial crack. For $c/a=0$, the special cases of a completely free, sectorial, thick plate and cylinder are formed. The 3-D vibrations of V-notched cylindrical elastic solids are classified into two groups, namely, on the one hand, V-notched *plates* having $a/h=20$ (thin) [34], $a/h=10$ (moderately thick) [36], and $a/h=5$ (thick), and on the other hand, V-notched *cylinders* with $h/a=2, 4, 6,$ and 10. Here, the cylinders of $h/a=6$ and 10 may be considered as V-notched and cracked slender *rods*—for which newly published 3-D vibration solutions are presented herein extending the work of Leissa and So [23,24], So and Leissa [25], and other recent investigations [30,49] discussed herein—and for which a wider range of newly published results by the present writers are to appear.

It is important to determine whether stress singularities along the reentrant terminus edge of a V-notch must be explicitly taken into consideration to obtain accurate vibration solutions. To clearly understand the phenomenology and nature of the 3-D normal and transverse shear stress singularities existing along the V-notch terminus edge, normalized contour plots of vibratory in-plane and transverse displacements are presented for a thick circular plate with a sharp notch (i.e., $5°$ notch angle), and for a cylinder with a sharp radial crack notch (i.e., $1°$ notch angle). Comparisons of free vibration characteristics are presented in this study between the results obtained by the methodology employed by the authors and previously published results obtained by alternative approaches to the solutions.

2. Method of analysis

As a classic problem of solid mechanics, the mensuration of an arbitrarily shaped cylindrical body was defined by Archimedes, who first put in plain words that the volume of any cylindrical solid was equal to the product of the area of its base into the height, h, of the solid, and that the area of the curved surface was equal to that of an arbitrarily shaped panel (e.g., a rectangular panel in the special case of a circular cylindrical solid) having two of its sides equal to the circumference of the arbitrarily shaped base and the other two sides equal to the height of the solid. The V-notched cylindrical solid shown in Fig. 1 is a surface traced out by a line, called a generatrix, that moves parallel to itself and passes through the circumference of a V-notched circular curve, $r(\theta)$, called a directrix. A generalization of this structural configuration further

proposed here is an arbitrarily shaped V-notched cylindrical solid, being a surface traced out by a family of generatrix, which pass through the circumference of an arbitrarily shaped V-notched directrix curve, $r(\theta)$, several of which are described in Appendix A (see Fig. A1). The axis of an arbitrarily shaped V-notched cylindrical solid is the line joining the centers of two V-notched arbitrarily shaped sections; it is the line through the center of the directrix, $r(\theta)$, parallel to the generators.

A continuum-based 3-D variational Ritz formulation for completely free cylindrical elastic solids having a V-notch (Fig. 1) is derived in cylindrical coordinates. No simplifying kinematic assumption are made on the strain distribution through the thickness of the elastic bodies, as typically used in rod, beam, plate and shell theories. The Ritz procedure is employed with two sets of admissible functions assumed for the in-plane u and v, and transverse w, vibratory displacements. The first set comprises mathematically complete algebraic–trigonometric polynomials, which guarantee convergence to exact frequency solutions, as sufficient solution sizes are retained. However, when a large size of polynomials is utilized, numerical ill-conditioning becomes an obstacle and prohibits one from achieving accurate solutions. Thus, a second set of edge functions [34] is employed, which account for tri-axial stress singularities along the terminus edge of a reentrant V-notch or sharp radial crack of an elastic solid.

Strain energy of the 3-D V-notched cylindrical elastic solid (Fig. 1) is given by the volume integral,

$$V = \frac{1}{2} \int \int \int [\Lambda(\varepsilon_r + \varepsilon_\theta + \varepsilon_z)^2 + 2G(\varepsilon_r^2 + \varepsilon_\theta^2 + \varepsilon_z^2) + G(\gamma_{r\theta}^2 + \gamma_{rz}^2 + \gamma_{\theta z}^2)]r(\theta)\,dr\,d\theta\,dz, \tag{1}$$

where we have incorporated in the above and hereafter, an assumed arbitrary radial coordinate variable function, $r=r(\theta)$, and where Λ and G are Lamé constants

$$\Lambda = \frac{vE}{(1 + v)(1 - 2v)}, G = \frac{E}{2(1 + v)}. \tag{2}$$

E is Young's modulus, and v is Poisson's ratio.

In terms of 3-D elastic solid displacement components (u_r, v_θ, w_z), the strain–displacement equations are defined as

$$\varepsilon_r = \frac{\partial u_r}{\partial r}, \; \varepsilon_{r\theta} = \frac{1}{2}\left(\frac{1}{r(\theta)}\frac{\partial u_r}{\partial \theta} - \frac{v_\theta}{r(\theta)} + \frac{\partial v_\theta}{\partial r}\right),$$

$$\varepsilon_\theta = \frac{1}{r(\theta)}\frac{\partial v_\theta}{\partial \theta} + \frac{u_r}{r(\theta)}, \; \varepsilon_{rz} = \frac{1}{2}\left(\frac{\partial w_z}{\partial r} + \frac{\partial u_r}{\partial z}\right),$$

$$\varepsilon_z = \frac{\partial w_z}{\partial z}, \; \varepsilon_{\theta z} = \frac{1}{2}\left(\frac{\partial v_\theta}{\partial z} + \frac{1}{r(\theta)}\frac{\partial w_z}{\partial \theta}\right), \tag{3}$$

where u_r and v_θ are in-plane displacements along the radial and circumferential directions, respectively, and w_z is the transverse displacement. During vibration the kinetic energy of the 3-D V-notched cylindrical elastic solid (Fig. 1) is given by the volume integral

$$T = \frac{\rho}{2} \int \int \int (\dot{u}_r^2 + \dot{v}_\theta^2 + \dot{w}_z^2)r(\theta)\,dr\,d\theta\,dz, \tag{4}$$

where ρ is the mass per unit volume and the dots represent time derivatives.

Assuming simple harmonic motions in time t, as follows:

$$u_r(r, \theta, z) = U_r(r, \theta, z)e^{i\omega t},$$

$$v_\theta(r, \theta, z) = V_\theta(r, \theta, z)e^{i\omega t},$$

$$w_z(r, \theta, z) = W_z(r, \theta, z)e^{i\omega t}. \tag{5}$$

In Eq. (5) only $i = \sqrt{-1}$ and the vector set (U_r, V_θ, W_z) are 3-D displacement amplitude functions corresponding to the vibratory circular frequency (ω) (in rad/s) of a cylindrical solid having a V-notch.

Assuming maximum displacements in a vibratory cycle and introducing under this condition Eqs. (5) into Eqs. (1)–(4), the maximum strain and kinetic energies, V_{max} and T_{max}, respectively, during a vibratory cycle are, as follows:

$$V_{max} = \frac{1}{2} \int \int \int \left\{ (\Lambda + 2G)\left[\left(\frac{\partial U_r}{\partial r}\right)^2 + \left(\frac{\partial W_z}{\partial z}\right)^2 + \frac{1}{r(\theta)^2}\left(U_r + \frac{\partial V_\theta}{\partial \theta}\right)^2\right] + 2\Lambda\left[\frac{\partial U_r}{\partial r}\frac{\partial W_z}{\partial z} + \frac{1}{r(\theta)}\left(U_r + \frac{\partial V_\theta}{\partial \theta}\right)\left(\frac{\partial U_r}{\partial r} + \frac{\partial W_z}{\partial z}\right)\right] \right.$$

$$\left. + \frac{G}{r(\theta)^2}\left[\left(\frac{\partial U_r}{\partial \theta} + r(\theta)\frac{\partial V_\theta}{\partial r} - V_\theta\right)^2 + \left(r(\theta)\frac{\partial V_\theta}{\partial z} + \frac{\partial W_z}{\partial \theta}\right)^2\right] + G\left(\frac{\partial U_r}{\partial r} + \frac{\partial W_z}{\partial z}\right)^2 \right\}r(\theta)\,dr\,d\theta\,dz, \tag{6a}$$

$$T_{max} = \frac{\rho\omega^2}{2} \int \int \int (U_r^2 + V_\theta^2 + W_z^2)r(\theta)\,dr\,d\theta\,dz. \tag{6b}$$

The total energy functional required by the variational Ritz method and established upon substitution of Eqs. (6a and b) is

$$\Pi = V_{\max} - T_{\max}. \tag{7}$$

In Eqs. (6) and (7), the combined 3-D symmetric and anti-symmetric spatial trial functions for the in-plane displacements (U_r, V_θ) and transverse displacement (W_z) are

$$U_r(r,\theta,z) = \sum_{i=1}^{L} a_i \xi_i(r,\theta,z) = U_r^s + U_r^a = U_{r_p}^s + U_{r_e}^s + U_{r_p}^a + U_{r_e}^a,$$

$$V_\theta(r,\theta,z) = \sum_{i=1}^{M} b_i \zeta_i(r,\theta,z) = V_\theta^s + V_\theta^a = V_{\theta_p}^s + V_{\theta_e}^s + V_{\theta_p}^a + V_{\theta_e}^a,$$

$$W_z(r,\theta,z) = \sum_{i=1}^{M} c_i \varphi_i(r,\theta,z) = W_z^s + W_z^a = W_{z_p}^s + W_{z_e}^s + W_{z_p}^a + W_{z_e}^a, \tag{8}$$

where in the above, a_i, b_i, and c_i represent collectively adjustable coefficients associated with ξ_i, ζ_i, and φ_i, which are hybrid series of admissible approximate displacement fields, comprised of mathematically complete algebraic–trigonometric polynomials (indicated by the subscripted (p)) and edge functions (indicated by the subscripted (e)), described later and particularly suitable through inherent symmetries (indicated by the superscripted symmetric (s) and anti-symmetric (a) notations) for the 3-D vibratory displacements of thick circular plates and cylinders having a V-notch or sharp radial crack. Minimizing the total energy functional (Eq. (7)) with respect to the generalized coefficients of Eqs. (8) leads to the following matrix set of linear homogeneous algebraic equations, recast as a standard eigenvalue problem for the jth characteristic circular frequency, ω_j, corresponding to the jth characteristic vector of generalized coefficients, $[\{a_i\}^{\mathrm{T}}, \{b_i\}^{\mathrm{T}}, \{c_i\}^{\mathrm{T}}]_j^{\mathrm{T}}$:

$$\frac{\partial(V_{\max} - T_{\max})}{\partial a_i} = 0, \quad \frac{\partial(V_{\max} - T_{\max})}{\partial b_i} = 0, \quad \frac{\partial(V_{\max} - T_{\max})}{\partial c_i} = 0,$$

$$\left(\begin{bmatrix} [K_{ij}^{aa}] & [K_{ij}^{ab}] & [K_{ij}^{ac}] \\ & [K_{ij}^{bb}] & [K_{ij}^{bc}] \\ \text{sym.} & & [K_{ij}^{cc}] \end{bmatrix} - \omega_j^2 \begin{bmatrix} [M_{ij}^{aa}] & [0] & [0] \\ & [M_{ij}^{bb}] & [0] \\ \text{sym.} & & [M_{ij}^{cc}] \end{bmatrix} \right) \begin{Bmatrix} \{a_i\} \\ \{b_i\} \\ \{c_i\} \end{Bmatrix}_j = \begin{Bmatrix} \{0\} \\ \{0\} \\ \{0\} \end{Bmatrix}, \tag{9}$$

in which the coefficients for the elastic stiffness $[K_{ij}]$ are defined as follows:

$$K_{ij}^{aa} = \int \int \int \left[(\Lambda + 2G)\left(r(\theta)\frac{\partial \xi_i}{\partial r}\frac{\partial \xi_j}{\partial r} + \frac{1}{r(\theta)}\xi_i \xi_j \right) + \Lambda\left(\frac{\partial \xi_i}{\partial r}\xi_j + \xi_i\frac{\partial \xi_j}{\partial r} \right) + G\left(\frac{1}{r(\theta)}\frac{\partial \xi_i}{\partial \theta}\frac{\partial \xi_j}{\partial \theta} + r(\theta)\frac{\partial \xi_i}{\partial z}\frac{\partial \xi_j}{\partial z} \right) \right] dr\, d\theta\, dz,$$

$$K_{ij}^{ab} = \int \int \int \left[\frac{(\Lambda + 2G)}{r(\theta)}\xi_i\frac{\partial \zeta_j}{\partial \theta} + \Lambda\frac{\partial \xi_i}{\partial r}\frac{\partial \zeta_j}{\partial \theta} + G\left(\frac{\partial \xi_i}{\partial \theta}\frac{\partial \zeta_j}{\partial r} - \frac{1}{r(\theta)}\frac{\partial \xi_i}{\partial \theta}\zeta_j \right) \right] dr\, d\theta\, dz,$$

$$K_{ij}^{ac} = \int \int \int \left[\Lambda\left(r(\theta)\frac{\partial \xi_i}{\partial r}\frac{\partial \varphi_j}{\partial z} + \xi_i\frac{\partial \varphi_j}{\partial z} \right) + G\left(r(\theta)\frac{\partial \xi_i}{\partial z}\frac{\partial \varphi_j}{\partial r} \right) \right] dr\, d\theta\, dz,$$

$$K_{ij}^{bb} = \int \int \int \left[\frac{(\Lambda + 2G)}{r(\theta)}\frac{\partial \zeta_i}{\partial \theta}\frac{\partial \zeta_j}{\partial \theta} + G\left(r(\theta)\frac{\partial \zeta_i}{\partial r}\frac{\partial \zeta_j}{\partial r} - \frac{\partial \zeta_i}{\partial r}\zeta_j - \zeta_i\frac{\partial \zeta_j}{\partial r} + \frac{1}{r(\theta)}\zeta_i \zeta_j + r(\theta)\frac{\partial \zeta_i}{\partial z}\frac{\partial \zeta_j}{\partial z} \right) \right] dr\, d\theta\, dz,$$

$$K_{ij}^{bc} = \int \int \int \left(\Lambda\frac{\partial \zeta_i}{\partial \theta}\frac{\partial \varphi_j}{\partial z} + G\frac{\partial \zeta_i}{\partial z}\frac{\partial \varphi_j}{\partial \theta} \right) dr\, d\theta\, dz,$$

$$K_{ij}^{cc} = \int \int \int \left[(\Lambda + 2G)\left(r(\theta)\frac{\partial \varphi_i}{\partial z}\frac{\partial \varphi_j}{\partial z} \right) + G\left(\frac{1}{r(\theta)}\frac{\partial \varphi_i}{\partial \theta}\frac{\partial \varphi_j}{\partial \theta} + r(\theta)\frac{\partial \varphi_i}{\partial r}\frac{\partial \varphi_j}{\partial r} \right) \right] dr\, d\theta\, dz, \tag{10}$$

and the coefficients for the inertial mass $[M_{ij}]$ are defined as

$$M_{ij}^{aa} = \rho \int \int \int r(\theta)\xi_i \xi_j \, dr\, d\theta\, dz,$$

$$M_{ij}^{bb} = \rho \int \int \int r(\theta)\zeta_i \zeta_j \, dr\, d\theta\, dz,$$

$$M_{ij}^{cc} = \rho \int \int \int r(\theta)\varphi_i \varphi_j \, dr\, d\theta\, dz. \tag{11}$$

The vanishing determinant of the algebraic equations (9) yields a set of eigenvalues (natural frequencies), which are subsequently expressed in terms of the non-dimensional frequency parameter $\omega a^2 \sqrt{\rho h/D}$, commonly used in the plate vibration literature (*Note*: $\omega a^2 \sqrt{\rho h/D}$ is employed for the sake of uniformity and comparison of results across the wide range of idealizations of V-notched cylindrical bodies, including thin and thick V-notched plates (a/h=5–20), albeit for the wide range of cylinders (h/a=2–10) examined herein, variations in $\omega a^2 \sqrt{\rho/E}$ could also be a more useful parameter to observe, or even still, variations in $\omega a \sqrt{\rho/G}$ employed by others [49]. Eigenvectors involving the generalized coefficients $\{a_i\}$, $\{b_i\}$, and $\{c_i\}$ may be determined in the usual manner by substituting the eigenvalues back into the homogeneous equations (9). These resulting eigenvectors of generalized coefficients are then substituted back into Eqs. (8) to calculate normalized in-plane and transverse displacement modal contours of V-notched cylindrical elastic bodies. In this work, these modal contours are normalized at the middle surface of the V-notched plates with respect to the maximum in-plane and transverse displacement components (i.e., $-1 \leq U_r/U_{r_{max}} \leq 1$, $-1 \leq V_\theta/V_{\theta_{max}} \leq 1$, and $-1 \leq W_z/W_{z_{max}} \leq 1$, whereas for visualizing and comparing the V-notched cylinder mode shapes, the modal contours are normalized at the top surface of the cracked cylinder with respect to the maximum in-plane and transverse displacement components.

For a cylindrical elastic solid having a V-notch or sharp radial crack, values of $r(\theta)$ in Eqs. (9)–(11), defining the stress-free circumferential face (as shown by the variable location of the assumed cylindrical coordinates in Fig. 1), is explicitly θ-dependent and thus, a new generalized numerical volume integration procedure was developed in the present work to perform the complicated volume integrals in Eqs. (9)–(11). For completeness and generality of the present formulation to arbitrarily shaped cylindrical elastic solids with V-notches and sharp radial cracks, the volume integrals in Eqs. (9)–(11) have been generalized and accurately carried out for six representative domains using the values of $r(\theta)$ given in Eqs. (A.1)–(A.6c) in Appendix A. Classical Chaldni-type laboratory observations and findings [1] reveal vibration characteristics of circular and arbitrarily shaped elastic solids modeled as plates yield largely similar nodal patterns, albeit the non-dimensional frequencies may differ depending on the elastic solid shape. Such Chaldni-type nodal pattern observations do not generalize as similar relationships between V-notched circular cylindrical elastic solids and V-notched arbitrarily shaped elastic solids. Moreover, the additional formulations of $r=r(\theta)$ in Appendix A generalize Eqs. (9)–(11) of the present analysis for future follow-on extensions used by other investigators to examine 3-D vibrations of arbitrarily shaped V-notched thick plates and generally shaped V-notched elastic bodies.

The 3-D displacement amplitude functions for the vibrations of a completely free cylindrical elastic solid having a V-notch or sharp radial crack are assumed as the sum of two finite series: (i) admissible, mathematically complete, algebraic–trigonometric polynomials and (ii) admissible edge functions.

For the symmetric 3-D vibration modes, displacement trial functions are assumed as

$$U_r^s = U_{r_p}^s + U_{r_e}^s,$$

$$V_\theta^s = V_{\theta_p}^s + V_{\theta_e}^s,$$

$$W_z^s = W_{z_p}^s + W_{z_e}^s, \tag{12}$$

where $U_{r_p}^s$, $V_{\theta_p}^s$, $W_{z_p}^s$ are the admissible and mathematically complete set of symmetric algebraic–trigonometric polynomials and $U_{r_e}^s$, $V_{\theta_e}^s$, $W_{z_e}^s$ are admissible symmetric edge functions, which account for singular stress behavior along the re-entrant terminus edge of the V-notch (Fig. 1). In Eqs. (12), the symmetric algebraic–trigonometric polynomial functions are written as

$$U_{r_p}^s(r,\theta,z) = \sum_{i=2,4}^{I_1} \sum_{j=0,2,4}^{i} \sum_{k=0}^{K_1} A_{ijk}^s r^{i-1} \cos(j\theta) z^k + \sum_{i=1,3,5}^{I_2} \sum_{j=1,3,5}^{i} \sum_{k=0}^{K_2} A_{ijk}^s r^{i-1} \cos(j\theta) z^k,$$

$$V_{\theta_p}^s(r,\theta,z) = \sum_{i=2,4}^{I_3} \sum_{j=2,4}^{i} \sum_{k=0}^{K_3} B_{ijk}^s r^{i-1} \sin(j\theta) z^k + \sum_{i=1,3,5}^{I_4} \sum_{j=1,3,5}^{i} \sum_{k=0}^{K_4} B_{ijk}^s r^{i-1} \sin(j\theta) z^k,$$

$$W_{z_p}^s(r,\theta,z) = \sum_{i=2,4}^{I_5} \sum_{j=0,2,4}^{i} \sum_{k=0}^{K_5} C_{ijk}^s r^{i} \cos(j\theta) z^k + \sum_{i=1,3,5}^{I_6} \sum_{j=1,3,5}^{i} \sum_{k=0}^{K_6} C_{ijk}^s r^{i-1} \cos(j\theta) z^k, \tag{13}$$

in which A_{ijk}^s, B_{ijk}^s, and C_{ijk}^s are undetermined coefficients in a_i, b_i, and c_i (Eqs. (8)), and the values of i, j, and k are specially chosen to avoid unacceptable stress singularities at r=0, and yet preserve the mathematical completeness of the resulting series. Thus, convergence to the exact frequencies is guaranteed, when this series is employed in the present Ritz procedure.

The displacement polynomials in Eqs. (13) should theoretically yield accurate frequencies even for a completely free cylindrical elastic solid having a V-notch or sharp radial crack, where stress singularities exists at the terminus reentrant edge. However, the number of terms required may be computationally prohibitive. This problem is alleviated by augmentation of the displacement algebraic–trigonometric polynomial trial set for the symmetric 3-D modes with admissible symmetric edge functions [34], which introduce the proper 3-D singular vibratory stresses along the terminus

edge formed by the free radial faces. The set of symmetric edge functions is taken as

$$U^s_{r_e}(r,\theta,z) = \sum_{m=1}^{M_1}\sum_{k=0}^{K_1}(\text{Re}[U^s_{r_{mk}}(r,\theta,z)] + \text{Im}[U^s_{r_{mk}}(r,\theta,z)]),$$

$$V^s_{\theta_e}(r,\theta,z) = \sum_{m=1}^{M_2}\sum_{k=0}^{K_2}(\text{Re}[V^s_{\theta_{mk}}(r,\theta,z)] + \text{Im}[V^s_{\theta_{mk}}(r,\theta,z)]),$$

$$W^s_{z_e}(r,\theta,z) = \sum_{m=1}^{M_3}\sum_{k=0}^{K_3}W^{K_3}_{z_{mk}}(r,\theta,z), \tag{14}$$

where $U^s_{r_{mk}}$, $V^s_{\theta_{mk}}$, $W^s_{z_{mk}}$ are the symmetric edge function series, which have been derived by McGee et al. [34].

Essentially therein, the characteristic equations and the corresponding edge functions are derived for a 3-D elastic sectorial solid having both radial faces completely free, satisfying the stress free radial face conditions. Advantage of the inherent symmetry is taken by choosing θ such that the boundaries are at $\theta = \pm\alpha/2$. Then, the solution of the eigensystem may be divided into its symmetric and anti-symmetric parts, which is adopted in the present work, and yielding the edge functions employed herein. As a result, the characteristic equations for free-free radial face conditions are [34]

$$\sin\lambda_m\alpha = \mp\lambda_m\sin\alpha, \tag{15a}$$

$$\sin(\overline{\lambda}_m)\frac{\alpha}{2} = 0, \quad (\text{sym.}),$$

$$\cos(\overline{\lambda}_m)\frac{\alpha}{2} = 0, \quad (\text{antisym.}). \tag{15b}$$

For the characteristic values, λ_m, obtained by solving the characteristic Eqs. (15) (the minus sign $(-)$ in Eq (15a) corresponding to the symmetric modes), the symmetric in-plane displacements, $U^s_{r_{mk}}$, $V^s_{\theta_{mk}}$, is

For symmetric modes

$$U^s_{r_{mk}}(r,\theta,z) = \sum_{m=1}^{\infty}\sum_{k=0}^{\infty}r^{\lambda_m}C_{mk}\left\{-\frac{\varsigma_{2m}\cos(\lambda_m-1)\dfrac{\alpha}{2}}{\cos(\lambda_m+1)\dfrac{\alpha}{2}}\cos(\lambda_m+1)\theta + \cos(\lambda_m-1)\theta\right\}z^k, \tag{16a}$$

$$V^s_{\theta_{mk}}(r,\theta,z) = \sum_{m=1}^{\infty}\sum_{k=0}^{\infty}r^{\lambda_m}C_{mk}\left\{\frac{\varsigma_{2m}\cos(\lambda_m-1)\dfrac{\alpha}{2}}{\cos(\lambda_m-1)\dfrac{\alpha}{2}}\sin(\lambda_m+1)\theta - \beta_m\sin(\lambda_m-1)\theta\right\}z^k, \tag{16b}$$

where given v is Poisson's ratio, then

$$\varsigma_{2m} = \frac{\lambda_m+1}{\lambda_m-3+4v}, \beta_m = \frac{\lambda_m+3-4v}{\lambda_m-3+4v}, \tag{16c}$$

and for the characteristic values $\overline{\lambda}_m$ (Eq. (15b)), the transverse displacement, $W^s_{z_{mk}}$, is

$$W^s_{z_{mk}}(r,\theta,z) = \sum_{m=1}^{\infty}\sum_{k=0}^{\infty}r^{\overline{\lambda}_m}G_{mk}(\cos\overline{\lambda}_m\theta)z^k. \tag{16d}$$

and C_{mk} and G_{mk} are arbitrary generalized coefficients in a_i, b_i, and c_i (Eqs. (8)). Similarly, for the 3-D anti-symmetric vibration modes, the trial displacement functions are

$$U^a_r = U^a_{r_p} + U^a_{r_e},$$
$$V^a_\theta = V^a_{\theta_p} + V^a_{\theta_e},$$
$$W^a_z = W^a_{z_p} + W^a_{z_e}, \tag{17}$$

where the anti-symmetric algebraic–trigonometric polynomial functions are

$$U^a_{r_p}(r,\theta,z) = \sum_{i=2,4}^{I_1}\sum_{j=2,4}^{i}\sum_{k=0}^{K_1}A^a_{ijk}r^{i-1}\sin(j\theta)z^k + \sum_{i=1,3,5}^{I_2}\sum_{j=1,3,5}^{i}\sum_{k=0}^{K_2}A^a_{ijk}r^{i-1}\sin(j\theta)z^k,$$

$$V^a_{\theta_p}(r,\theta,z) = \sum_{i=2,4}^{I_3}\sum_{j=0,2,4}^{i}\sum_{k=0}^{K_3}B^a_{ijk}r^{i-1}\cos(j\theta)z^k + \sum_{i=1,3,5}^{I_4}\sum_{j=1,3,5}^{i}\sum_{k=0}^{K_4}B^a_{ijk}r^{i-1}\cos(j\theta)z^k,$$

$$W^a_{z_p}(r,\theta,z) = \sum_{i=2,4}^{I_5}\sum_{j=2,4}^{i}\sum_{k=0}^{K_5}C^a_{ijk}r^{i}\sin(j\theta)z^k + \sum_{i=1,3,5}^{I_6}\sum_{j=1,3,5}^{i}\sum_{k=0}^{K_6}C^a_{ijk}r^{i}\sin(j\theta)z^k, \tag{18}$$

in which A_{ijk}^a, B_{ijk}^a and C_{ijk}^a are undetermined coefficients in a_i, b_i, and c_i (Eqs. (8)), Similarly, as in Eqs. (13), the values of i, j, and k are specially chosen to avoid unacceptable stress singularities at $r=0$, and yet preserve the mathematical completeness of the resulting series. The corresponding anti-symmetric edge functions are

$$U_{r_e}^a(r,\theta,z) = \sum_{m=1}^{M_1}\sum_{k=0}^{K_1}(\text{Re}[U_{r_{mk}}^a(r,\theta,z)] + \text{Im}[U_{r_{mk}}^a(r,\theta,z)]),$$

$$V_{\theta_e}^a(r,\theta,z) = \sum_{m=1}^{M_2}\sum_{k=0}^{K_2}(\text{Re}[V_{\theta_{mk}}^a(r,\theta,z)] + \text{Im}[V_{\theta_{mk}}^a(r,\theta,z)]),$$

$$W_{z_e}^a(r,\theta,z) = \sum_{m=1}^{M_3}\sum_{k=0}^{K_3}W_{z_{mn}}^a(r,\theta,z), \tag{19}$$

where $U_{r_{mk}}^a$, $V_{\theta_{mk}}^a$, $W_{z_{mk}}^a$ have been developed elsewhere [34], resulting in

For anti-symmetric modes

$$U_{r_{mk}}^a(r,\theta,z) = \sum_{m=1}^{\infty}\sum_{k=0}^{\infty} r^{\lambda_m} D_{mk}\left\{-\frac{\varsigma_{2m}\sin(\lambda_m-1)\frac{\alpha}{2}}{\sin(\lambda_m+1)\frac{\alpha}{2}}\sin(\lambda_m+1)\theta + \sin(\lambda_m-1)\theta\right\}z^k, \tag{20a}$$

$$V_{\theta_{mk}}^a(r,\theta,z) = \sum_{m=1}^{\infty}\sum_{k=0}^{\infty} r^{\lambda_m} D_{mk}\left\{\frac{\varsigma_{2m}\sin(\lambda_m-1)\frac{\alpha}{2}}{\sin(\lambda_m+1)\frac{\alpha}{2}}\cos(\lambda_m+1)\theta + \beta_m\cos(\lambda_m-1)\theta\right\}z^k, \tag{20b}$$

$$W_{z_{mk}}^a(r,\theta,z) = \sum_{m=1}^{\infty}\sum_{k=0}^{\infty} r^{\bar{\lambda}_m} G_{mk}(\sin\bar{\lambda}_m\theta)z^k. \tag{20c}$$

and D_{mk} and G_{mk} are arbitrary generalized coefficients in a_i, b_i, and c_i (Eqs. (8)). The characteristic values λ_m of the above anti-symmetric in-plane displacements, $U_{r_{mk}}^s, V_{\theta_{mk}}^s$, are obtained by solving the characteristic Eqs. (15) (the minus sign (+) in Eq. (15a) corresponding to the anti-symmetric modes).

Each of the symmetric functions (Eqs. (16a)–(16c)) and anti-symmetric functions (Eqs. (20a)–(20c)) serve as assumed *edge functions* corresponding to the 3-D intersection of two free radial faces. Analogous to classically thin plates [33,44–46] and Mindlin plates [47,36,43], 3-D edge functions characterize the local stress distribution, which can be singular along a terminus edge formed at the reentrant corner formed by the two intersecting radial faces [34].

Edge functions are grouped in order of increasing magnitude of the corresponding λ_m and $\bar{\lambda}_m$. For a complex λ the real and imaginary parts of the corresponding complex edge functions are used as independent functions (i.e., Eqs. (14), (16a,b), (19) and (20a,b)). The transverse edge functions (i.e., Eqs. (16c) and (20c)) are ordered by real $\bar{\lambda}$ only. The solutions of λ_m in Eqs. (15a) may be complex numbers, and to find the required numbers of λ_m in sequence based on the magnitude of λ_m, the subroutine ZANLY in IMSL is used. However, the characteristic equations for $\bar{\lambda}_m$ in Eqs. (15b) have exact solutions which are for the symmetric modes,

$$\bar{\lambda}_m = \frac{2m\pi}{\alpha} \ (m=1,2,3,\ldots) \quad \text{for all } \alpha, \tag{21a}$$

and for the anti-symmetric modes,

$$\bar{\lambda}_m = \frac{2\left(m-\frac{1}{2}\right)\pi}{\alpha} \ (m=1,2,3,\ldots) \quad \text{for all } \alpha. \tag{21b}$$

From Eqs. (21), one can see that the transverse shear stresses (τ_{rz} and $\tau_{\theta z}$) along the terminus of a V-notch having free radial faces vary as $r^{\pi/\alpha}$ for all α as shown in Ref. [34].

The 3-D stresses along the V-notch terminus edge ($r=0$) become infinite (i.e., singular) for $0<\lambda_m<1$ and $0<\bar{\lambda}_m<1$. For $\lambda_m>1$, no normal (σ_r, σ_θ, and σ_z) and in-plane shear ($\tau_{r\theta}$) stress singularities exist along the V-notch terminus edge. For $\bar{\lambda}_m>1$, the singular transverse shear stresses (τ_{rz} and $\tau_{\theta z}$) are not present along the terminus edge. The chart summarizes the smallest characteristic values of λ_m and $\bar{\lambda}_m$ used in the 3-D edge functions given in Eqs. (15) and (21) for various terminus angles (α). Here, use of the edge functions in conjunction with the algebraic–trigonometric polynomials

allows proper representation of the terminus edge stress singularities for the free vibration of the completely free notched elastic solids.

α (deg)	λ_m		$\overline{\lambda}_m$	
	S^*	A^{**}	S^*	A^{**}
270	0.544	0.909	1.333	0.667
300	0.512	0.731	1.200	0.600
330	0.501	0.598	1.091	0.545
350	0.500	0.529	1.029	0.514
355	0.500	0.514	1.014	0.507
359	0.500	0.503	1.003	0.501

*Symmetric mode in θ.
**Anti-symmetric mode in θ.

It should be noticed that for symmetric modes (in the chart, the smallest $\overline{\lambda}_m > 1$), the edge functions do not account for the singular transverse shear stresses (τ_{rz} and $\tau_{\theta z}$) along the terminus edge of the V-notch [38].

3. Convergence studies

The 3-D Ritz formulation, as discussed, is employed to obtain reasonably convergent frequency solutions, as sufficient numbers of algebraic–trigonometric polynomials and 3-D edge functions are utilized. Substituting Eqs. (12)–(20) into Eqs. (9)–(11), a set of eigenvalue equations is established for symmetric mode and anti-symmetric mode in θ, respectively. The associated eigenvalue equations are particularly suitable for completely free circular plates and cylinders having a V-notch (Fig. 1).

Convergence studies are presented for completely free, thick circular plates (a/h=5) and cylinders (h/a=2) having V-notches with a 5° notch angle (360°−α, where α=355°) and having c/a of 0.75 and 0. Depicted in Fig. 2 are four representative configurations, which are examined in this work. These configurations are delineated by notch depths ranging from a shallow notch (c/a=0.75) to a very deep notch (c/a=−0.5). In all calculations, Poisson's ratio v has been set to 0.3. All of the frequency calculations in this work were performed on an IBM/RS-6000 970 power-server with an IBM 340 workstation cluster using extended precision (28 significant figure) arithmetic.

Table 1 presents the convergence studies on the first six non-dimensional frequency parameters $\omega a^2 \sqrt{\rho h/D}$ for a completely free thick (a/h=5) circular plate having a shallow notch (c/a=0.75) with a 5° notch angle (α=355°). Frequency results are obtained as 13×3, 14×3, 15×3, 16×3, and 17×3 polynomial solutions are used in conjunction with 0, 1×3, 5×3, 10×3, 15×3, and 17×3 3-D edge function solutions for each symmetry class in θ. The polynomial solution sizes describe the number of upper indices I_q and K_q, where q=1,2,…,6, in Eqs. (13) or (18). For each of the in-plane and transverse displacement functions, equal numbers for I_q (i.e., $I_1=I_2=\cdots=I_6$) and K_q (i.e., $K_1=K_2=\cdots=K_6$) were employed in all of the 3-D Ritz calculations. For example, a 13×3 solution size is defined by the upper indices I_q=13 and K_q=3 in Eqs. (13) or (18). Here, K_q=3 means that a four-term polynomial series is used in the thickness direction (z-direction). Equal sizes of edge functions (i.e., $M_1=M_2=M_3$ and $K_1=K_2=K_3$ in Eqs. (14) and (16) or (19)–(20)) were also used for the in-plane and transverse displacement fields. Note that a reasonably sufficient cubic (i.e., $K_1=K_2=K_3$=3, or four-term polynomial series) approximation in the z-direction was employed for the edge function trial sets as well as the polynomial trial sets to properly represent thick plate transverse shear behaviors and to ensure accurate solutions. It should be also noted that the first six modes are rigid body modes in the 3-D vibration of the completely free circular plates having V-notches. These rigid body frequencies, which are zero, are not shown in the tables.
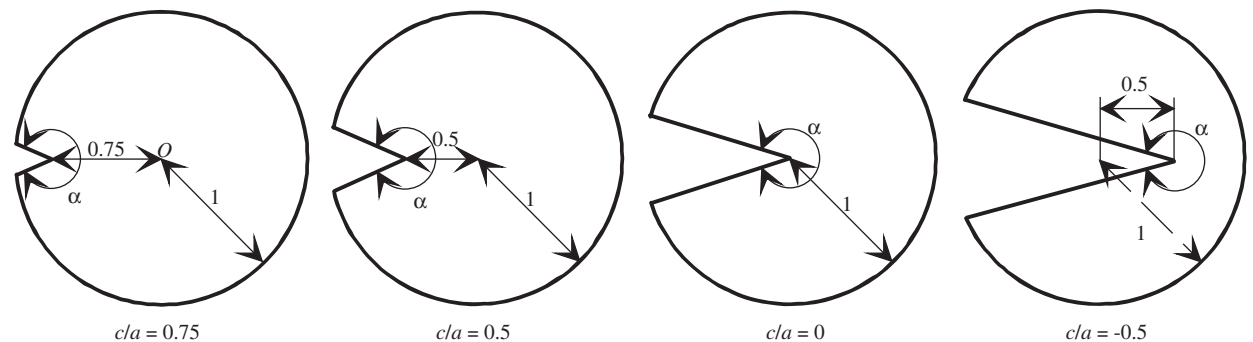
Fig. 2. V-notches with various depths.

c/a = 0.75 c/a = 0.5 c/a = 0 c/a = -0.5

Table 1
Convergence of frequency parameters $\omega a^2 \sqrt{\rho h/D}$ for a completely free thick circular plate having a V-notch (α=355°, c/a=0.75, a/h=5).

Mode no. (symmetry class[a])	Size of edge functions	Solution size of polynomials				
		13×3	14×3	15×3	16×3	17×3
1	0	5.118	5.118	5.118	5.118	5.118
(A)	1×3	5.062	5.061	5.060	5.059	5.058
	5×3	5.037	5.036	5.036	5.036	5.035
	10×3	5.037	5.036	5.036	5.035	5.035
	15×3	5.036	5.036	5.036	5.035	5.035
	17×3	5.036	5.036	5.036	5.035	[b]
2	0	5.125	5.125	5.125	5.125	5.125
(S)	1×3	5.054	5.053	5.052	5.051	5.050
	5×3	5.040	5.039	5.039	5.039	5.039
	10×3	5.039	5.039	5.039	5.039	5.038
	15×3	5.039	5.039	5.039	5.039	[b]
	17×3	5.039	5.039	5.039	[b]	[b]
3	0	8.523	8.523	8.523	8.523	8.523
(S)	1×3	8.479	8.479	8.478	8.477	8.477
	5×3	8.469	8.469	8.468	8.468	8.468
	10×3	8.469	8.468	8.468	8.468	8.468
	15×3	8.469	8.468	8.468	8.468	[b]
	17×3	8.469	8.468	8.468	[b]	[b]
4	0	11.33	11.33	11.33	11.33	11.33
(A)	1×3	11.05	11.05	11.05	11.04	11.03
	5×3	10.94	10.93	10.93	10.93	10.93
	10×3	10.93	10.93	10.93	10.93	10.93
	15×3	10.93	10.93	10.93	10.93	10.93
	17×3	10.93	10.93	10.93	10.93	[b]
5	0	11.35	11.35	11.35	11.35	11.35
(S)	1×3	11.11	11.10	11.10	11.10	11.10
	5×3	11.06	11.06	11.06	11.06	11.06
	10×3	11.06	11.06	11.06	11.06	11.06
	15×3	11.06	11.06	11.06	11.06	[b]
	17×3	11.06	11.06	11.06	[b]	[b]
6	0	18.06	18.06	18.06	18.06	18.06
(A)	1×3	17.91	17.90	17.89	17.88	17.87
	5×3	17.61	17.60	17.60	17.59	17.59
	10×3	17.60	17.60	17.59	17.59	17.59
	15×3	17.60	17.59	17.59	17.59	17.58
	17×3	17.60	17.59	17.59	17.59	[b]

[a] (S) symmetric mode in θ and (A) anti-symmetric mode in θ.
[b] No results due to matrix ill-conditioning.

Fig. 3. Convergence of fundamental frequency parameters for a completely free thick circular plate having a V-notch (α=355°, c/a=0.75, a/h=5).
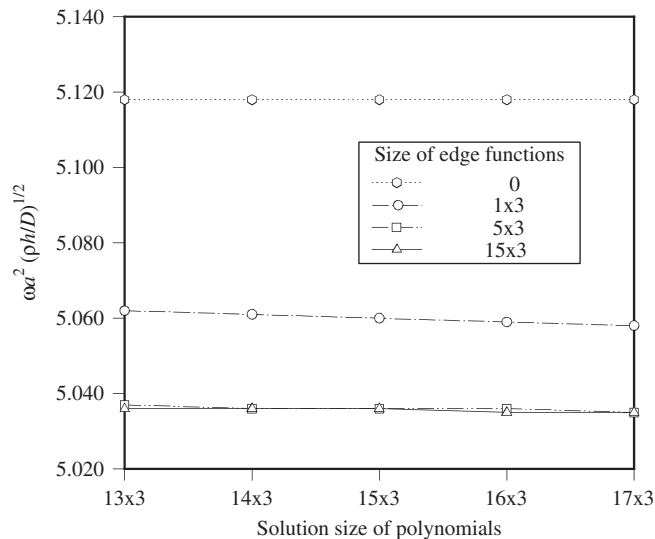
Table 2

Convergence of frequency parameters $\omega a^2 \sqrt{\rho h/D}$ for a completely free thick sectorial plate (α=355°, c/a=0, a/h=5).

Mode no. (symmetry class[a])	Size of edge functions	Solution size of polynomials				
		14×3	15×3	16×3	17×3	18×3
1	0	5.084	5.083	5.083	5.082	5.082
(A)	1×3	4.179	4.160	4.138	4.123	4.105
	5×3	2.625	2.620	2.618	2.615	2.614
	10×3	2.617	2.615	2.612	2.611	2.609
	20×3	2.615	2.613	2.611	2.610	2.608
	30×3	2.614	2.612	2.610	2.609	2.608
	40×3	2.614	2.612	2.610	2.609	2.607
2	0	5.144	5.143	5.143	5.142	5.141
(S)	1×3	4.335	4.312	4.296	4.278	4.265
	5×3	4.053	4.050	4.050	4.048	4.047
	10×3	4.049	4.047	4.046	4.045	4.045
	20×3	4.048	4.046	4.046	4.044	4.044
	30×3	4.048	4.046	4.046	4.044	4.044
	40×3	4.048	4.046	4.046	4.044	4.044
3	0	11.26	11.26	11.26	11.26	11.25
(A)	1×3	8.323	8.293	8.256	8.234	8.205
	5×3	7.175	7.173	7.171	7.169	7.168
	10×3	7.164	7.163	7.162	7.162	7.161
	20×3	7.163	7.162	7.161	7.161	7.160
	30×3	7.162	7.162	7.161	7.161	7.160
	40×3	7.162	7.162	7.161	7.161	7.160
4	0	8.508	8.506	8.505	8.504	8.503
(S)	1×3	7.482	7.464	7.452	7.438	7.428
	5×3	7.221	7.219	7.218	7.217	7.216
	10×3	7.218	7.216	7.216	7.215	7.214
	20×3	7.217	7.215	7.215	7.214	7.214
	30×3	7.217	7.215	7.215	7.214	7.214
	40×3	7.217	7.215	7.215	7.214	7.214
5	0	11.40	11.39	11.39	11.39	11.39
(S)	1×3	10.77	10.77	10.76	10.76	10.75
	5×3	10.58	10.58	10.58	10.58	10.57
	10×3	10.57	10.57	10.57	10.57	10.57
	20×3	10.57	10.57	10.57	10.57	10.57
	30×3	10.57	10.57	10.57	10.57	10.57
	40×3	10.57	10.57	10.57	10.57	10.57
6	0	17.98	17.98	17.98	17.98	17.98
(A)	1×3	13.52	13.50	13.48	13.46	13.45
	5×3	12.96	12.95	12.94	12.93	12.92
	10×3	12.89	12.89	12.89	12.88	12.88
	20×3	12.89	12.89	12.88	12.88	12.88
	30×3	12.89	12.89	12.88	12.88	12.87
	40×3	12.89	12.88	12.88	12.87	12.87

[a] (S) symmetric mode in θ and (A) anti-symmetric mode in θ.

In Table 1, consider the fundamental frequency mode which is an anti-symmetric one. The use of polynomial functions alone results in the upper-bound convergence to an inaccurate $\omega a^2 \sqrt{\rho h/D}$ value of 5.118. The trial set, consisting of the first edge function (corresponding to the lowest λ) along with as little as 13×3 polynomials, yields an upper-bound frequency value, which is much lower than the first row of $\omega a^2 \sqrt{\rho h/D}$ values obtained using no edge functions. An examination of the next five rows of data reveals that an accurate $\omega a^2 \sqrt{\rho h/D}$ value to four significant figures is 5.035. To clearly understand this behavior, the convergence of the fundamental frequency mode given in Table 1 is plotted in Fig. 3. A similar level of convergence accuracy can be seen for the higher modes. It is seen in Table 1 that as the solution sizes of the hybrid set of polynomials and edge functions increase, a slight deterioration in the overall convergence occurs due to the onset of matrix ill-conditioning and numerical round-off errors. Despite the ill-conditioning, a convergence to three or four significant figures is essentially achieved for the first six frequencies.

Table 2 explains the convergence of frequency parameter $\omega a^2 \sqrt{\rho h/D}$ for a thick (a/h=5) circular plate having a much deeper notch (c/a=0) and a 5° notch angle. In this case, the terminus of the V-notch is located at the plate center, resulting in a sectorial plate. If one compares the convergence of frequencies in Table 2 with those in Table 1 for the circular plate having a shallow notch effect (c/a=0.75), it is seen that for the deep notched plate, the convergence rate is slightly slower, requiring more edge functions to accurately obtain frequency data (i.e., four significant figures). Whereas adding a trial set

Table 3
Convergence of frequency parameters $\omega a^2 \sqrt{\rho h/D}$ for a completely free cylinder having a V-notch ($\alpha=355°$, $c/a=0.75$, $h/a=2$).

Mode no. (symmetry class[a])	Size of edge functions	Solution size of polynomials				
		4×8	5×8	6×8	7×8	8×8
1	0	1.610	1.610	1.610	1.610	1.610
(A)	1×8	1.567	1.565	1.564	1.563	1.562
	5×8	1.560	1.560	1.559	1.559	1.559
	10×8	1.560	1.559	1.559	1.559	1.559
	15×8	1.559	1.559	1.559	1.559	1.559
	20×8	1.559	1.559	1.559	1.559	1.559
2	0	2.028	2.028	2.027	2.027	2.027
(A)	1×8	1.997	1.996	1.994	1.993	1.993
	5×8	1.993	1.992	1.991	1.991	1.991
	10×8	1.992	1.992	1.991	1.991	1.991
	15×8	1.992	1.992	1.991	1.991	1.991
	20×8	1.992	1.992	1.991	1.991	1.991
3	0	2.031	2.031	2.030	2.030	2.030
(S)	1×8	2.026	2.026	2.025	2.024	2.024
	5×8	2.026	2.025	2.024	2.024	2.024
	10×8	2.025	2.025	2.024	2.024	2.024
	15×8	2.025	2.025	2.024	2.024	2.024
	20×8	2.025	2.025	2.024	2.024	2.024
4	0	2.048	2.042	2.042	2.042	2.042
(S)	1×8	2.033	2.026	2.025	2.025	2.025
	5×8	2.032	2.025	2.025	2.025	2.025
	10×8	2.032	2.025	2.025	2.025	2.025
	15×8	2.032	2.025	2.025	2.025	2.025
	20×8	2.032	2.025	2.025	2.025	2.025
5	0	2.049	2.043	2.043	2.043	2.043
(A)	1×8	2.041	2.035	2.035	2.035	2.034
	5×8	2.038	2.034	2.034	2.034	2.034
	10×8	2.038	2.034	2.034	2.033	2.033
	15×8	2.038	2.034	2.034	2.033	2.033
	20×8	2.038	2.034	2.034	2.033	2.033
6	0	2.208	2.204	2.204	2.204	2.204
(A)	1×8	2.182	2.177	2.176	2.176	2.176
	5×8	2.178	2.174	2.174	2.174	2.174
	10×8	2.178	2.174	2.174	2.174	2.174
	15×8	2.178	2.174	2.174	2.174	2.174
	20×8	2.178	2.174	2.174	2.174	2.174

[a] (S) symmetric mode in θ and (A) anti-symmetric mode in θ.

of 5×3 edge functions was sufficient to obtain frequencies accurate to three or four significant figures for $c/a=0.75$ (Table 1), additional edge functions (as many as 40×3) were required to achieve sufficient accuracy in some of the modes of the sectorial plate ($c/a=0$) (Table 2).

Convergence studies for shallow ($c/a=0.75$) and deep ($c/a=0$) notched cylinder ($h/a=2$) having a notch angle of $5°$ are shown in Tables 3 and 4, respectively. Frequency results are obtained as 4×8, 5×8, 6×8, 7×8 and 8×8 polynomial solutions along with 0, 1×8, 5×8, 10×8, 15×8, and 20×8 solutions of 3-D edge functions are utilized. Note that a reasonably sufficient seventh-order (i.e., eight-term) polynomial approximation in the z-direction was employed for the edge function trial sets as well as the algebraic–trigonometric polynomial trial sets to properly represent cylindrical elastic solid ($h/a=2$) transverse shear behaviors and to ensure accurate solutions. It should be also noted once again, like thick circular plates with V-notches, that the first six modes are rigid body modes in the 3-D vibration of the completely free cylindrical elastic solids having V-notches. These rigid body frequencies, which are zero, are not shown in the tables. Compared with the data for the thick plates listed in Tables 1 and 2, it is seen that the $\omega a^2 \sqrt{\rho h/D}$ convergence rate is much faster and the numerical approximating influence of the edge functions is greater. Interestingly, for the shallow notched cylinder (Table 3), a trial set consisting of the first edge function (corresponding to the lowest λ_m) along with 8×8 polynomials yields the converged $\omega a^2 \sqrt{\rho h/D}$ values accurate to three significant figures for all modes (except the sixth one). A four significant figures convergence of $\omega a^2 \sqrt{\rho h/D}$ is seen in Tables 3 and 4 for all modes, when 10×8 edge functions are retained in the present Ritz procedure.

A z-polynomial trial function convergence study was also performed, but the findings of this analysis are not shown for brevity. It was found that a cubic (i.e., four-term) approximation in the z-direction employed for the V-notched thick-plate vibrations findings, and a seventh-order (i.e., eight-term) approximation in the z-direction employed for the V-notched

Table 4
Convergence of frequency parameters $\omega a^2 \sqrt{\rho h / D}$ for a completely free cylinder having a V-notch (α=355°, c/a=0, h/a=2).

Mode no. (symmetry class[a])	Size of edge functions	Solution size of polynomials				
		4×8	5×8	6×8	7×8	8×8
1	0	2.040	2.038	2.038	2.038	2.038
(S)	1×8	0.723	0.720	0.719	0.719	0.718
	5×8	0.671	0.670	0.670	0.669	0.669
	10×8	0.671	0.670	0.669	0.669	0.669
	15×8	0.671	0.670	0.669	0.669	0.669
	20×8	0.671	0.670	0.669	0.669	0.669
2	0	1.608	1.608	1.608	1.608	1.607
(A)	1×8	0.846	0.837	0.831	0.829	0.826
	5×8	0.813	0.810	0.809	0.808	0.808
	10×8	0.810	0.809	0.808	0.808	0.807
	15×8	0.810	0.809	0.808	0.808	0.807
	20×8	0.810	0.809	0.808	0.808	0.807
3	0	2.046	2.040	2.039	2.038	2.038
(S)	1×8	1.093	1.080	1.077	1.073	1.071
	5×8	1.060	1.056	1.055	1.055	1.054
	10×8	1.059	1.056	1.055	1.054	1.054
	15×8	1.059	1.056	1.055	1.054	1.054
	20×8	1.059	1.055	1.055	1.054	1.054
4	0	2.016	2.015	2.014	2.013	2.013
(A)	1×8	1.603	1.592	1.585	1.582	1.580
	5×8	1.579	1.567	1.566	1.565	1.564
	10×8	1.574	1.565	1.564	1.564	1.564
	15×8	1.573	1.565	1.564	1.564	1.564
	20×8	1.573	1.565	1.564	1.564	1.564
5	0	2.055	2.047	2.047	2.047	2.047
(A)	1×8	1.653	1.644	1.640	1.636	1.634
	5×8	1.621	1.618	1.618	1.617	1.616
	10×8	1.619	1.617	1.617	1.616	1.616
	15×8	1.619	1.617	1.617	1.616	1.616
	20×8	1.619	1.617	1.617	1.616	1.616
6	0	2.200	2.191	2.190	2.190	2.819
(A)	1×8	1.866	1.855	1.852	1.850	1.849
	5×8	1.822	1.816	1.815	1.814	1.813
	10×8	1.819	1.815	1.814	1.813	1.813
	15×8	1.819	1.814	1.814	1.813	1.813
	20×8	1.819	1.814	1.814	1.813	1.813

[a] (S) symmetric mode in θ and (A) anti-symmetric mode in θ.

cylindrical elastic solids were sufficiently accurate. This was the case when employing the algebraic–trigonometric polynomial trial sets only (i.e., no edge functions). Nonetheless, the convergence acceleration of the edge functions using comparable (four-term or eight-term) z-direction polynomial approximation were substantial and more essential to the overall convergence rate of the hybrid trial sets compared in Tables 1–4, while at the same time properly representing transverse shear and rotary inertia effects on the accurate solutions resulting from the reentrant terminus edge singularities—the primary effect and focus of the present work. In the next section, sufficient comparisons of the present findings to previously published results in the literature also serve to validate the accuracy of the present findings.

4. Non-dimensional frequency solutions of V-notched circular plates and cylinders

Extensive convergence studies were performed to compile the least upper-bound frequency parameters $\omega a^2 \sqrt{\rho h / D}$ for the first six modes of thick (a/h=5) circular plates and cylinders (h/a=2) having V-notches with various α and c/a. These studies are summarized in Table 5 for the notched thick plates and in Table 6 for the notched cylinders, respectively. Frequency data corresponding to the anti-symmetric modes with respect to θ are indicated by an asterisk (*). All frequency results are guaranteed upper-bounds to the exact values (accurate to the four significant figures). The solutions sizes of polynomials (Eqs. (13) or (18)) and edge functions (Eqs. (14) and (16) or (19) and (20)) employed in Table 5 for the four significant figure frequency convergence of completely free thick (a/h=5) circular plates with V-notches are summarized in Chart A. The solutions sizes of polynomials (Eqs. (13) or (18)) and edge functions (Eqs. (14) and (16) or (19) and (20))

Table 5
Frequency parameters $\omega a^2 \sqrt{\rho h/D}$ for completely free thick (a/h=5) circular plates with V-notches.

α (deg)	c/a	Mode					
		1	2	3	4	5	6
90	0.75	6.511	8.292[a]	11.13	15.06[a]	17.37	22.76
	0.5	7.989	10.60[a]	13.86	18.02[a]	22.53	28.42
	0	14.14	19.80[a]	25.37	30.33[a]	36.98	42.62
	−0.5	38.54	52.59[a]	56.77	67.48[a]	73.31[a]	80.91[a]
180	0.75	5.202[a]	5.580	8.937	11.83[a]	12.42	17.91[a]
	0.5	5.733[a]	5.858	10.13	13.34[a]	14.37	17.68[a]
	0	6.561	8.585[a]	15.84[a]	15.90	19.67	24.21[a]
	−0.5	10.00	17.72[a]	18.55	24.17[a]	31.40	33.75[a]
270	0.75	5.022[a]	5.228	8.537	10.94[a]	11.60	17.86[a]
	0.5	4.713[a]	5.439	8.380	10.35[a]	12.55	17.44
	0	4.261[a]	5.616	8.642	11.35[a]	14.94[a]	16.37
	−0.5	4.594[a]	5.999	10.66	11.50[a]	16.25[a]	21.28
300	0.75	5.025[a]	5.151	8.506	10.91[a]	11.39	17.71[a]
	0.5	4.615[a]	5.212	8.276	9.762[a]	11.83	16.58[a]
	0	3.516[a]	5.140	7.817	9.605[a]	13.89	14.24[a]
	−0.5	2.995[a]	4.885	8.447	9.278[a]	12.31[a]	16.34[a]
330	0.75	5.030[a]	5.087	8.483	10.91[a]	11.20	17.63[a]
	0.5	4.565[a]	4.993	8.226	9.286[a]	11.16	15.46[a]
	0	2.961[a]	4.542	7.411	8.155[a]	11.90	13.62[a]
	−0.5	2.005[a]	3.082	7.286	7.605[a]	9.911[a]	12.64
350	0.75	5.034[a]	5.048	8.471	10.92[a]	11.09	17.59[a]
	0.5	4.549[a]	4.853	8.207	8.999[a]	10.74	14.76[a]
	0	2.672[a]	4.141	7.249	7.345[a]	10.82	13.05[a]
	−0.5	1.572[a]	3.194	6.832	6.693[a]	8.920[a]	10.81
355	0.75	5.035[a]	5.038	8.468	10.93[a]	11.06	17.58[a]
	0.5	4.546[a]	4.819	8.204	8.927[a]	10.64	14.58[a]
	0	2.607[a]	4.044	7.160[a]	7.214	10.57	12.87[a]
	−0.5	1.486[a]	3.059	6.488[a]	6.745	8.732[a]	10.43
359	0.75	5.031	5.036[a]	8.466	10.93[a]	11.04	17.58[a]
	0.5	4.544[a]	4.791	8.201	8.871[a]	10.56	14.44[a]
	0	2.559[a]	3.968	7.107[a]	7.186	10.39	12.72[a]
	−0.5	1.423[a]	2.956	6.330[a]	6.680	8.598[a]	10.13
Circular		5.119	5.119[a]	8.520	11.34[a]	11.340	18.06[a]

[a] Anti-symmetric modes θ.

employed to obtain in Table 6 the four significant figure frequency convergence of completely free cylinders (h/a=2) with V-notches is summarized in Chart B.

For various terminus angles (α) of the completely free V-notched thick (a/h=5) circular plates, some interesting trends can be seen in Table 5 regarding the variation of $\omega a^2 \sqrt{\rho h/D}$ as c/a decreases. It is clear that for α=330°, 350°, 355°, and 359°, the frequency values in the first six modes monotonically decrease with decreasing c/a. At α=300°, a reversal of the above cited trends develops quite significantly. For instance, the fundamental values of $\omega a^2 \sqrt{\rho h/D}$ in this case monotonically decrease with decreasing c/a, while some of the higher mode values of $\omega a^2 \sqrt{\rho h/D}$ are increased with decreasing c/a. At small terminus angle (α=270°), a similar frequency increase with notch depth is observed in all modes. The frequency increase is more substantial for plates with α=90° and for semi-circular plates (α=180°) as c/a is decreased. Clearly, the plates with α=90° and 180° do not form a V-notch. Nonetheless, the $\omega a^2 \sqrt{\rho h/D}$ values for α=90° do indicate some interesting new vibration solutions for the special cases of thick segmented plates with decreasing c/a (Fig. 4), for which no previously published frequency results are known to exist. For a c/a value of 0.5, 0, and −0.5, $\omega a^2 \sqrt{\rho h/D}$ is seen in Table 5 to be significantly decreased as the terminus angle α is increased. At c/a=0.75, the frequency changes with increasing α are less dramatic and largely unpredictable; that is, they sometimes display an increase or a decrease with increasing α, depending on the symmetry associated with the mode.

The frequency data listed in Table 5 are compared with the data for a complete circular thick plate obtained by using the present 3-D analysis. For the case of a sharp, shallow crack (i.e., c/a=0.75 and α=359°), the crack reduces the frequencies of the symmetric modes 1, 3, and 5 by 1.72, 0.63, and 2.65 percent, respectively, and those of the anti-symmetric modes 2, 4, and 6 by 1.62, 3.62, and 2.66 percent, respectively. In general, it is shown in Table 5 that the presence of a V-notch (i.e., $\alpha \geq 270°$) decreases the fundamental frequency of a completely free thick circular plate, and that shallow notches (c/a=0.75) cause approximately the same decrease (1.7–1.9 percent), regardless of the terminus angle. A sharp notch ($\alpha \geq 330°$) or

Table 6

Frequency parameters $\omega a^2 \sqrt{\rho h/D}$ for completely free cylinders (h/a=2) with V-notches.

α (deg)	c/a	Mode					
		1	2	3	4	5	6
90	0.75	1.508[a]	1.885	1.975[a]	2.275	2.344[a]	2.459
	0.5	1.472[a]	1.774	1.924[a]	2.468[a]	2.493	2.515
	0	1.387[a]	1.457	1.726[a]	2.548	2.724[a]	2.771
	−0.5	0.916	1.265[a]	1.273[a]	2.123	2.535[a]	2.583
180	0.75	1.551[a]	1.976	2.052[a]	2.062[a]	2.140	2.197[a]
	0.5	1.428[a]	1.862	2.066[a]	2.123[a]	2.179	2.325
	0	1.179[a]	1.556	2.012[a]	2.058	2.191	2.219[a]
	−0.5	0.863[a]	1.011	1.695[a]	1.914	1.993	1.998[a]
270	0.75	1.564[a]	1.991[a]	2.019	2.043[a]	2.068	2.179[a]
	0.5	1.393[a]	1.820	1.945[a]	2.015	2.026[a]	2.101
	0	0.977[a]	1.102	1.439	1.854[a]	1.908	1.922[a]
	−0.5	0.606	0.623	0.971	1.454[a]	1.539	1.732[a]
300	0.75	1.564[a]	1.991[a]	2.023	2.040[a]	2.051	2.177[a]
	0.5	1.383[a]	1.727	1.912[a]	1.944	2.015[a]	2.080
	0	0.913[a]	0.913	1.274	1.815[a]	1.849[a]	1.947[a]
	−0.5	0.430	0.562[a]	0.828	1.359[a]	1.584[a]	1.598[a]
330	0.75	1.562[a]	1.991[a]	2.025	2.036	2.036[a]	2.175[a]
	0.5	1.371[a]	1.616	1.865	1.885[a]	2.003[a]	2.071
	0	0.765	0.853[a]	1.143	1.708[a]	1.732[a]	1.851[a]
	−0.5	0.320	0.504	0.737	1.166[a]	1.397[a]	1.626[a]
350	0.75	1.560[a]	1.991[a]	2.025	2.026	2.034[a]	2.174[a]
	0.5	1.362[a]	1.538	1.806	1.870[a]	1.996[a]	2.065
	0	0.687	0.816[a]	1.070	1.593[a]	1.639[a]	1.819[a]
	−0.5	0.272	0.469[a]	0.692	1.054[a]	1.302[a]	1.598[a]
355	0.75	1.559[a]	1.991[a]	2.024	2.025	2.033[a]	2.174[a]
	0.5	1.359[a]	1.518	1.790	1.866[a]	1.995[a]	2.064
	0	0.669	0.807[a]	1.054	1.564[a]	1.616[a]	1.813[a]
	−0.5	0.262	0.461[a]	0.682	1.029[a]	1.281[a]	1.594[a]
359	0.75	1.559[a]	1.991[a]	2.022	2.025	2.033[a]	2.173[a]
	0.5	1.357[a]	1.502	1.777	1.863[a]	1.993[a]	2.062
	0	0.656	0.800[a]	1.041	1.540[a]	1.598[a]	1.808[a]
	−0.5	0.255	0.455[a]	0.674	1.009[a]	1.265[a]	1.591[a]
Circular		1.610[a]	2.027[a]	2.027	2.043	2.043[a]	2.204[a]

[a] Anti-symmetric modes θ.

crack is seen further to decrease all first six frequencies from those of the complete circular plate. A notch of large angle (i.e., smaller α, such as $\alpha \leq 300°$) causes a decrease in the fundamental frequency, but the higher frequencies may be decreased by the notch. For such modes, the decreased mass of the plate is more significant than its decreased stiffness.

In Table 6, it is seen that for the completely free V-notched (i.e., $\alpha \geq 270°$) cylinders (h/a=2), the frequency parameters $\omega a^2 \sqrt{\rho h/D}$ in the first six modes decrease with decreasing c/a. For cylinders with α=90° and for semi-circular cylinders (α=180°), the fundamental values of $\omega a^2 \sqrt{\rho h/D}$ decrease with decreasing c/a, whereas some of the higher mode values of $\omega a^2 \sqrt{\rho h/D}$ increase with decreasing c/a. It should be noted that the cylinders with α=90° and 180° do not form a V-notch. The frequency data for α=90° do indicate some interesting special cases of segmented cylinders with decreasing c/a (Fig. 4), for which no previously published frequency results are known to exist. For a c/a value of 0.5, 0, and −0.5, the frequency parameters $\omega a^2 \sqrt{\rho h/D}$ are seen in Table 6 to decrease, as the terminus angle α is increased, except in the second and third modes for α=180°. For the cylinders with a shallow notch (c/a=0.75), the frequency changes with increasing α are less dramatic and largely unpredictable; that is, as seen for the thick circular plates with a shallow notch, the frequency parameters $\omega a^2 \sqrt{\rho h/D}$ of the shallow-notched cylinders sometimes exhibit an increase or a decrease with increasing α, depending on the symmetry associated with the mode.

The frequency data listed in Table 6 are compared with the data for a complete circular cylinder obtained by using the present 3-D analysis. For the case of a sharp, shallow crack (i.e., c/a=0.75 and α=359°), the crack reduces the frequencies of the symmetric modes 3 and 4 by 0.25 and 0.88 percent, respectively, and those of the anti-symmetric modes 1, 2, 5, and 6 by 3.17, 1.78, 0.49, and 1.41 percent, respectively. In general, it is shown in Table 6 that the presence of a V-notch reduces the fundamental frequency of complete circular cylinders, and that the presence of a shallow notches (c/a=0.75) cause approximately the same decrease within the range of 2.9–3.2 percent.

α (degrees)	c/a	Polynomials	Edge Functions
90, 180	0.75	18×3	0
	0.5	18×3	0
	0	18×3	0
	-0.5	18×3	0
270	0.75	18×3	2×3 (1×3)*
	0.5	18×3	2×3 (1×3)
	0	18×3	2×3 (1×3)
	-0.5	18×3	2×3 (1×3)
300	0.75	18×3	4×3 (2×3)
	0.5	18×3	4×3 (2×3)
	0	18×3	4×3 (2×3)
	-0.5	18×3	4×3 (2×3)
330	0.75	18×3	10×3 (5×3)
	0.5	18×3	10×3 (5×3)
	0	18×3	10×3 (5×3)
	-0.5	18×3	10×3 (5×3)
350	0.75	17×3 (18×3)	10×3
	0.5	18×3	10×3
	0	17×3	40×3
	-0.5	17×3	40×3
355, 359	0.75	17×3 (18×3)	10×3
	0.5	18×3	10×3 (20×3)
	0	18×3	40×3
	-0.5	18×3	40×3

Chart A. Solutions sizes of polynomials (Eq. (13) or (18)) and edge functions (Eqs. (14) and (16) or (19) and (20)) employed in Table 5. ( )*: solution size for anti-symmetric modes in θ.

5. Comparison studies

Comparisons are made in Tables 7 and 8 for frequency parameters $\omega a^2 \sqrt{\rho h/D}$ of shallow-notched (c/a=0.75) circular plates with a notch angle of 5° and complete circular plates, having a/h=20, 10, and 5. Table 7 lists $\omega a^2 \sqrt{\rho h/D}$ values for the symmetric modes in θ, whereas Table 8 presents $\omega a^2 \sqrt{\rho h/D}$ values for the anti-symmetric modes in θ. Frequency results obtained by the present 3-D method are compared with those recently reported in a classical thin plate Ritz analysis [33] and those produced by using a Mindlin plate theory [35,36,43]. The frequency solutions for the Mindlin plates were obtained using two different shear correction factor, namely $\kappa^2 = \pi^2/12$ [35] and $\kappa^2 = \frac{5}{6}$ [48]. Table 9 presents percent differences between frequencies from the Mindlin plate theory [36,43] and the present 3-D results.

In Mindlin plate theory [36,43], bending moments and transverse shear forces at the vertex of a V-notch vary as $r^{\lambda_k - 1}$ and $r^{\overline{\lambda}_k}$, respectively. The moments in the region of the vertex (r=0) become infinite (i.e., singular) for $0 < \lambda_k < 1$ (obtained from [36] using characteristic equations akin to Eqs. (15) shown herein). The singular transverse shear forces at r=0 exist for $-1 < \overline{\lambda}_k < 0$. For $\lambda_k > 1$ and $\overline{\lambda}_k > 0$, no singular moments and shear forces exist at the vertex of the V-notch. For $0 < \lambda_k < 1$ and $-1 < \overline{\lambda}_k < 0$, use of the Mindlin corner functions in conjunction with the algebraic–trigonometric polynomials permits proper representation of the reentrant corner stress singularities for the vibration of the completely free Mindlin circular plate having the V-notch. For α=355°, the smallest $\overline{\lambda}_k$ of the symmetric mode is 0.014 [36]. Here, the corner functions do not account for the singular shear forces at the reentrant vertex of the V-notch.

Similarly, according to the 3-D elasticity theory, tri-axial stresses along the V-notch terminus edge (r=0) become singular for $0 < \lambda_m < 1$ and $0 < \overline{\lambda}_m < 1$ (see Eqs. (15)). For $\lambda_m > 1$, normal (σ_r, σ_θ, and σ_z) and in-plane shear ($\tau_{r\theta}$) stress singularities are not present along the V-notch terminus edge. For $\overline{\lambda}_m > 1$, no singular transverse shear stresses (τ_{rz} and $\tau_{\theta z}$) exist along the terminus edge. For α=355°, the smallest $\overline{\lambda}_m$ of symmetric mode is 1.014 [34]. Here, the 3-D edge functions do not account for the singular transverse shear stresses along the reentrant terminus edge of the V-notch and these functions

α (degrees)	c/a	Polynomials	Edge Functions
90, 180	0.75	8×8	0
	0.5	8×8	0
	0	8×8	0
	-0.5	8×8	0
270	0.75	8×8	2×8 (1×8)*
	0.5	8×8	2×3 (1×8)
	0	8×8	2×8 (1×8)
	-0.5	8×8	2×8 (1×8)
300	0.75	8×8	4×8 (2×8)
	0.5	8×8	4×8 (2×8)
	0	8×8	4×8 (2×8)
	-0.5	8×8	4×8 (2×8)
330	0.75	8×8	10×8 (5×8)
	0.5	8×8	10×8 (5×8)
	0	8×8	10×8 (5×8)
	-0.5	8×8	10×8 (5×8)
350	0.75	8×8	10×8
	0.5	8×8	10×8
	0	8×8	20×8
	-0.5	8×8	20×8
355, 359	0.75	8×8	10×8
	0.5	8×8	20×8
	0	8×8	20×8
	-0.5	8×8	20×8

Chart B. Solutions sizes of polynomials (Eq. (13) or (18)) and edge functions (Eqs. (14) and (16) or (19) and (20)) employed in Table 6. ( )*: solution size for anti-symmetric modes in θ.

are only admissible. Fig. 5 depicts polynomial spaces approximated in the present Ritz procedure. It should be noticed in Fig. 5 that the mathematically complete algebraic–trigonometric polynomials are necessary and sufficient for the convergence of the Ritz procedure, whereas comparison functions (i.e., corner/edge functions) that satisfy both geometric and natural boundary conditions are sufficient, but not necessary for the convergence of the Ritz analysis. The admissible singularity functions (hatched portion in Fig. 5), which explicitly account for the reentrant corner/edge stress singularities, is the metric of the present solution.

In Tables 7 and 8, it is seen that the present 3-D elasticity-based theory gives substantially lower $\omega a^2 \sqrt{\rho h/D}$ values than those of the classical plate theory, even for large thickness ratio of a/h=20, due to the inherent shear deformation and rotary inertia. The present 3-D $\omega a^2 \sqrt{\rho h/D}$ values, however, have favorable agreement with $\omega a^2 \sqrt{\rho h/D}$ values obtained by the Mindlin plate theory [36,43]. The influence of shear forces is reflected in the potential energy of the present 3-D and Mindlin plate theory [36,43], whereas such forces are inherently absent from the potential energy derived from the classical plate theory. For the notched plates, the percent differences between the 3-D $\omega a^2 \sqrt{\rho h/D}$ values and Mindlin $\omega a^2 \sqrt{\rho h/D}$ values (using Reissner's κ^2=5/6) are only between 0.04 and 0.40 percent (Table 9).

Interestingly, the frequency percentage differences between the present 3-D and Mindlin theories are seen in Table 9 to be higher in the anti-symmetric modes than those in the symmetric modes. It is also seen in Table 9 that for the anti-symmetric modes, the frequency percentage differences of the notched plates are slightly more pronounced than those of the complete circular plates. As discussed previously, for the symmetric modes (here, the smallest $\bar{\lambda} > 0$ and the smallest $\bar{\lambda} > 1$), corner/edge functions do not account for transverse shear stress singularities at the re-entrant vertex/terminus of the V-notch. The shear stress singularities do not also exist for the circular plates. Clearly, one can see that the transverse
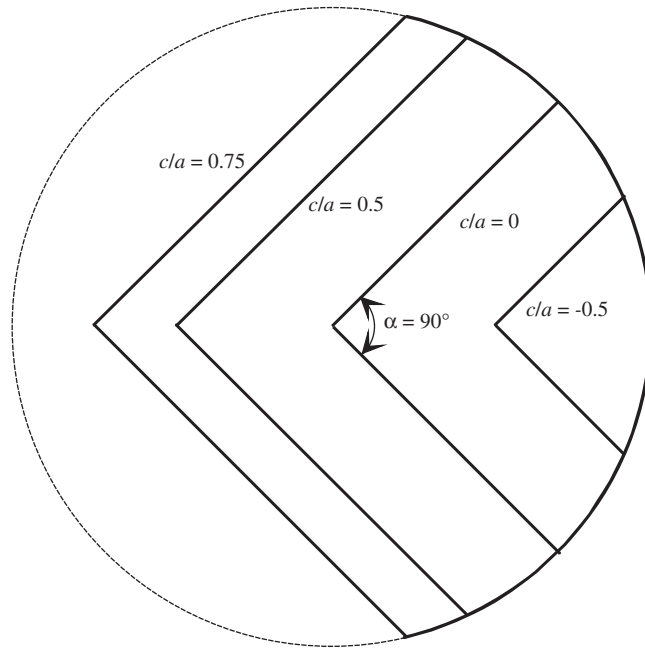
Fig. 4. Plate with α=90° and various c/a ratios.

Table 7
Comparison of frequency parameters $\omega a^2 \sqrt{\rho h/D}$ for completely free circular plates having a V-notch with symmetric modes in θ (c/a=0.75).

a/h	Mode no.	α=355°				Circular			
		CPT[a]	MPT[b]		3D[c]	CPT[a]	MPT[b]		3D[c]
			$\pi^2/12$[d]	5/6[d]			$\pi^2/12$[d]	5/6[d]	
20	1	5.298	5.262	5.262	5.266	5.358	5.330	5.330	5.330
	2	8.969	8.929	8.929	8.933	9.003	8.969	8.969	8.970
	3	12.20	12.05	12.05	12.06	12.44	12.31	12.31	12.32
10	1	5.298	5.202	5.203	5.204	5.358	5.278	5.278	5.279
	2	8.969	8.822	8.823	8.827	9.003	8.868	8.869	8.872
	3	12.20	11.78	11.78	11.79	12.44	12.06	12.07	12.07
5	1	5.298	5.033	5.035	5.038	5.358	5.114	5.116	5.119
	2	8.969	8.453	8.456	8.468	9.003	8.505	8.508	8.520
	3	12.20	11.03	11.04	11.06	12.44	11.31	11.32	11.34

[a] Classical thin plate theory [33].
[b] Mindlin plate theory [36,43].
[c] Present 3-D elasticity theory.
[d] Shear correction factor, κ^2.

shear singularities derived from the 3-D elasticity theory and Mindlin plate theory do not contribute to the frequency convergence for the symmetric modes.

Similar comparisons are made in Tables 10 and 11 for frequency parameters $\omega a^2 \sqrt{\rho h/D}$ for deep (c/a=0) notched plates with a notch angle of 5° and a/h=20, 10, and 5. Symmetric mode $\omega a^2 \sqrt{\rho h/D}$ values are listed in Table 10 and the anti-symmetric $\omega a^2 \sqrt{\rho h/D}$ values are shown in Table 11. Also given in Table 12, are percent differences between the $\omega a^2 \sqrt{\rho h/D}$ values calculated using the Mindlin plate theory [36,43] and the present 3-D elasticity-based analysis. As would be expected, it is seen in Tables 10 and 11 that the classical plate theory gives substantially higher $\omega a^2 \sqrt{\rho h/D}$ values than those of the present 3-D and Mindlin theories. The frequency parameters $\omega a^2 \sqrt{\rho h/D}$ obtained from the present 3-D elasticity theory and the Mindlin plate theory [36,43] are in close agreement. For the sectorial plates (c/a=0), the percent differences between the 3-D $\omega a^2 \sqrt{\rho h/D}$ values and Mindlin $\omega a^2 \sqrt{\rho h/D}$ values (using κ^2=5/6) are seen in Table 12 to be only between 0.14 and 0.51 percent.

Table 8
Comparison of frequency parameters $\omega a^2 \sqrt{\rho h/D}$ for completely free circular plates having a V-notch with anti-symmetric modes in θ (c/a=0.75).

a/h	Mode no.	α=355°				Circular			
		CPT[a]	MPT[b]		3D[c]	CPT[a]	MPT[b]		3D[c]
			$\pi^2/12$[d]	5/6[d]			$\pi^2/12$[d]	5/6[d]	
20	1	5.286	5.263	5.263	5.265	5.358	5.330	5.330	5.330
	2	12.10	11.99	11.99	12.01	12.44	12.31	12.31	12.32
	3	20.27	20.07	20.07	20.10	20.48	20.26	20.26	20.27
10	1	5.286	5.201	5.201	5.204	5.358	5.278	5.278	5.279
	2	12.10	11.69	11.69	11.70	12.44	12.06	12.07	12.07
	3	20.27	19.41	19.41	19.45	20.48	19.71	19.72	19.74
5	1	2.286	5.028	5.030	5.035	5.358	5.114	5.116	5.119
	2	12.10	10.89	10.90	10.93	12.44	11.31	11.32	11.34
	3	20.27	17.49	17.51	17.58	20.48	17.98	17.99	18.06

[a] Classical thin plate theory [33].
[b] Mindlin plate theory [36,43].
[c] Present 3-D elasticity theory.
[d] Shear correction factor, κ^2.

Table 9
Percent frequency differences of completely free circular plates having a V-notch between 3-D elasticity theory and Mindlin plate theory (α=355°, c/a=0.75).

a/h	Mode no.	Notched				Circular			
		S[a]		A[b]		S[a]		A[b]	
		3D-M[c]	3D-M[d]	3D-M[c]	3D-M[d]	3D-M[c]	3D-M[d]	3D-M[c]	3D-M[d]
20	1	0.08	0.08	0.04	0.04	0.00	0.00	0.00	0.00
	2	0.04	0.04	0.17	0.17	0.01	0.01	0.08	0.08
	3	0.08	0.08	0.15	0.15	0.08	0.08	0.05	0.05
10	1	0.04	0.02	0.06	0.06	0.02	0.02	0.02	0.02
	2	0.06	0.05	0.09	0.09	0.05	0.03	0.08	0.00
	3	0.08	0.08	0.21	0.21	0.08	0.00	0.15	0.10
5	1	0.10	0.06	0.14	0.10	0.10	0.06	0.10	0.06
	2	0.18	0.14	0.37	0.27	0.18	0.14	0.26	0.18
	3	0.27	0.18	0.51	0.40	0.26	0.18	0.44	0.39

[a] Symmetric mode in θ.
[b] Anti-symmetric mode in θ.
[c] Mindlin plate theory using κ^2=$\pi^2/12$.
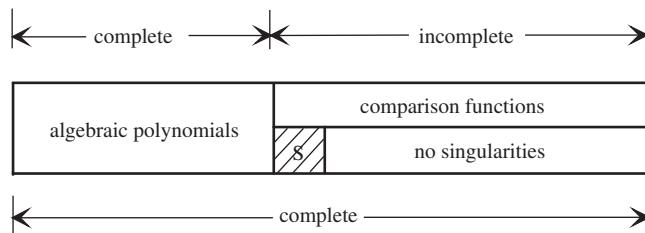[d] Mindlin plate theory using κ^2=5/6.

Fig. 5. Polynomial approximation space.

Tables 13 and 14 present the first six frequency parameters $\omega a^2 \sqrt{\rho h/D}$ of completely free and cantilevered solid rods and cylinders having a deep radial crack (i.e., c/a=0 and α=359°), respectively, for h/a=2, 4, 6, and 10. Here, the cylinders of h/a=6 and 10 may be considered as V-notched and cracked slender *rods*—for which newly published 3-D vibration solutions are given in Tables 13 and 14, extending the work of Leissa and So [23,24] and So and Leissa [25]. For all h/a ratios, converged frequencies of a cracked solid rod or cylinder are obtained as 8×8 polynomial trial solutions are used in

Table 10

Comparison of frequency parameters $\omega a^2 \sqrt{\rho h/D}$ for completely free sectorial plates with symmetric modes in θ (c/a=0).

a/h	Mode no.	α=355°				Circular			
		CPT[a]	MPT[b]		3D[c]	CPT[a]	MPT[b]		3D[c]
			$\pi^2/12$[d]	5/6[d]			$\pi^2/12$[d]	5/6[d]	
20	1	4.383	4.316	4.316	4.324	5.358	5.330	5.330	5.330
	2	7.746	7.673	7.673	7.682	9.003	8.969	8.969	8.970
	3	11.58	11.46	11.46	11.47	12.44	12.31	12.31	12.32
10	1	4.383	4.228	4.229	4.235	5.358	5.278	5.278	5.279
	2	7.746	7.548	7.549	7.556	9.003	8.868	8.869	8.872
	3	11.58	11.23	11.23	11.24	12.44	12.06	12.07	12.07
5	1	4.383	4.037	4.038	4.044	5.358	5.114	5.116	5.119
	2	7.746	7.200	7.203	7.214	9.003	8.505	8.508	8.520
	3	11.58	10.55	10.56	10.57	12.44	11.31	11.32	11.34

[a] Classical thin plate theory [33].
[b] Mindlin plate theory [36,43].
[c] Present 3-D elasticity theory.
[d] Shear correction factor, κ^2.

Table 11

Comparison of frequency parameters $\omega a^2 \sqrt{\rho h/D}$ for completely free sectorial plates with anti-symmetric modes in θ (c/a=0).

a/h	Mode no.	α=355°				Circular			
		CPT[a]	MPT[b]		3D[c]	CPT[a]	MPT[b]		3D[c]
			$\pi^2/12$[d]	5/6[d]			$\pi^2/12$[d]	5/6[d]	
20	1	2.822	2.805	2.806	2.817	5.358	5.330	5.330	5.330
	2	7.839	7.747	7.748	7.761	12.44	12.31	12.31	12.32
	3	15.18	14.88	14.88	14.93	20.48	20.26	20.26	20.27
10	1	2.822	2.729	2.730	2.744	5.358	5.278	5.278	5.279
	2	7.839	7.577	7.579	7.588	12.44	12.06	12.07	12.07
	3	15.18	14.29	14.30	14.33	20.48	19.71	19.72	19.74
5	1	2.822	2.594	2.596	2.607	5.358	5.114	5.116	5.119
	2	7.839	7.146	7.150	7.160	12.44	11.31	11.32	11.34
	3	15.18	12.81	12.82	12.88	20.48	17.98	17.99	18.06

[a] Classical thin plate theory [33].
[b] Mindlin plate theory [36,43].
[c] Present 3-D elasticity theory.
[d] Shear correction factor, κ^2.

conjunction with 20 × 8 trial sets of 3-D edge functions. For the cantilevered solid rods and cylinders, the z^k series indices were simply and appropriately adjusted to k=1,2,3,… in Eqs. (12)–(20) to ensure the proper kinematic conditions of the restrained end at z=0 was satisfied, producing the proper admissibility of the hybrid series of algebraic–trigonometric polynomials and edge functions employed in calculating the solutions.

In Tables 13 and 14, the frequency results for the cracked solid rods and cylinders are compared with those predicted for completely circular solid rods and cylinders (i.e., no crack). Extending Hutchinson's infinite circular cylinder solution based on the technique of variables separation, Mofakhamia et al. [49] recently offered a general solution as a semi-analytical series to analyze the vibration of finite solid and hollow circular cylinders with various end conditions, namely completely free and clamped ends. Specifically, the 3-D Navier displacement equations governing the motion of an isotropic solid media was transformed to scalar and vector potentials using a Helmholtz decomposition, and then through separation of variables, obtain an ordinary and modified Bessel functions series solution. The Mofakhamia et al. [49] general solution for the scalar and vector potentials was used to analyze the wave propagation of infinite or finite circular cylinders. Benchmarking against the general solution for the scalar and vector potentials investigated by Gazis [5] for infinite circular cylinders, the Mofakhamia et al. [49] closed-form solutions yielded more coefficients in their truncated series evaluation of free vibration characteristics of finite circular cylinders with various end conditions. In contrast to Hutchinson's studies on the vibration of free-end circular cylinders, additional series terms were also suggested by Mofakhamia et al. [49] to be included in the solution of the infinite cylinders. In the Mofakhamia ordinary and modified Bessel series, general end conditions were approximately satisfied using an orthogonalization technique. The general semi-analytical Bessel solution

Table 12
Percent frequency differences of completely free sectorial plates between 3-D elasticity theory and Mindlin plate theory (α=355°, c/a=0).

a/h	Mode no.	Sectorial				Circular			
		S[a]		A[b]		S[a]		A[b]	
		3D-M[c]	3D-M[d]	3D-M[c]	3D-M[d]	3D-M[c]	3D-M[d]	3D-M[c]	3D-M[d]
20	1	0.19	0.19	0.43	0.39	0.00	0.00	0.00	0.00
	2	0.12	0.12	0.18	0.17	0.01	0.01	0.08	0.08
	3	0.09	0.09	0.33	0.33	0.08	0.08	0.05	0.05
10	1	0.17	0.14	0.55	0.51	0.02	0.02	0.02	0.02
	2	0.11	0.09	0.14	0.12	0.05	0.03	0.08	0.00
	3	0.09	0.09	0.28	0.21	0.08	0.00	0.15	0.10
5	1	0.17	0.15	0.50	0.42	0.10	0.06	0.10	0.06
	2	0.19	0.15	0.20	0.14	0.18	0.14	0.26	0.18
	3	0.19	0.05	0.54	0.47	0.26	0.18	0.44	0.39

[a] Symmetric mode in θ.
[b] Anti-symmetric mode in θ.
[c] Mindlin plate theory using $\kappa^2 = \pi^2/12$.
[d] Mindlin plate theory using $\kappa^2 = 5/6$.

Table 13
Frequency parameters $\omega a^2 \sqrt{\rho h/D}$ for completely free solid rods and cylinders with a radial crack (c/a=0).

h/a	Mode no.	Symmetric mode in θ			Anti-symmetric mode in θ		
		α=359°	Circular		α=359°	Circular	
		3D[a]	3D[a]	3D[b]	3D[a]	3D[a]	3D[b]
2	1	0.656	2.027	2.027	0.800	1.610	1.610
	2	1.041	2.043	2.043	1.540	2.027	2.027
	3	1.916	2.204	2.204	1.598	2.043	2.043
4	1	0.332	0.396	0.397	0.278	0.396	0.397
	2	0.395	0.639	0.639	0.358	0.402	0.402
	3	0.402	0.733	0.733	0.604	0.733	0.733
6	1	0.138	0.138	0.138	0.128	0.138	0.138
	2	0.222	0.287	0.287	0.131	0.179	0.179
	3	0.244	0.298	0.298	0.267	0.298	0.298
10	1	0.034	0.034	0.034	0.032	0.034	0.034
	2	0.082	0.082	0.082	0.048	0.064	0.064
	3	0.104	0.104	0.104	0.075	0.082	0.082

[a] Present 3-D elasticity theory.
[b] Leissa and So [23,24]; So and Leissa [25]; Zhou et al. [30]; and Mofakhamia et al. [49].

covered various cases of finite length cylinders, such as rods and cylinders with various end conditions. Compared with previously developed Bessel series solutions, highly accurate and converged non-dimensional frequencies were reported in Mofakhamia et al. [49] using smaller solution matrices. Exact non-dimensional frequency ratios from the Mofakhamia series were reported with an error tolerance of 0.00001.

Numerical prediction agreement up to four significant figures for frequency parameters $\omega a^2 \sqrt{\rho h/D}$ for completely free solid rods and cylinders with no a radial crack (c/a=0) are posted in Table 13 (Poisson's ratio assumed as 0.3). It is shown that the results obtained from the present 3-D elasticity-based Ritz analysis are in good agreement with those obtained using previously developed methods. It can be inferred that up to four significant figure accurate frequency parameters $\omega a^2 \sqrt{\rho h/D}$ has been achieved amongst previously published 3-D elasticity closed-form solutions of Hutchinson and El-Azhari [21], and Mofakhamia et al. [49] and amongst previously published 3-D elasticity-based Ritz solutions of Leissa and So [23,24], So and Leissa [25], and Zhou et al. [30].

It is seen in Tables 13 and 14 that the frequency reductions due to the length scale of a radial crack are generally less significant as h/a ratios increase. In Table 13, the maximum frequency reduction of 67.6 percent due to the radial crack appears in the first symmetric mode for the completely free thick cylinders having h/a=2. For a completely free slender rod having h/a=10, symmetric frequency reductions due to the presence of the radial crack are negligible. Whereas, for the slender rod (h/a=10), a crack decreases the frequencies of the anti-symmetric modes by 5.9, 25.0, and 8.5 percent,

Table 14
Frequency parameters $\omega a^2 \sqrt{\rho h/D}$ for cantilevered solid rods and cylinders with a radial crack (c/a=0).

h/a	Mode no.	Symmetric mode in θ			Anti-symmetric mode in θ		
		α=359°	Circular		α=359°	Circular	
		3D[a]	3D[a]	3D[b]	3D[a]	3D[a]	3D[b]
2	1	0.515	0.518	0.518	0.458	0.518	0.518
	2	0.868	1.318	1.318	0.731	0.805	0.805
	3	1.317	1.479	1.480	1.409	1.479	1.480
4	1	0.082	0.082	0.082	0.076	0.082	0.082
	2	0.327	0.328	0.328	0.171	0.202	0.202
	3	0.332	0.333	0.333	0.303	0.333	0.333
6	1	0.026	0.026	0.026	0.025	0.026	0.026
	2	0.124	0.124	0.124	0.073	0.089	0.089
	3	0.145	0.145	0.145	0.113	0.124	0.124
10	1	0.006	0.006	0.006	0.006	0.006	0.006
	2	0.032	0.032	0.032	0.025	0.032	0.032
	3	0.052	0.052	0.052	0.031	0.032	0.032

[a] Present 3-D elasticity theory.
[b] Leissa and So [23,24] and So and Leissa [25].
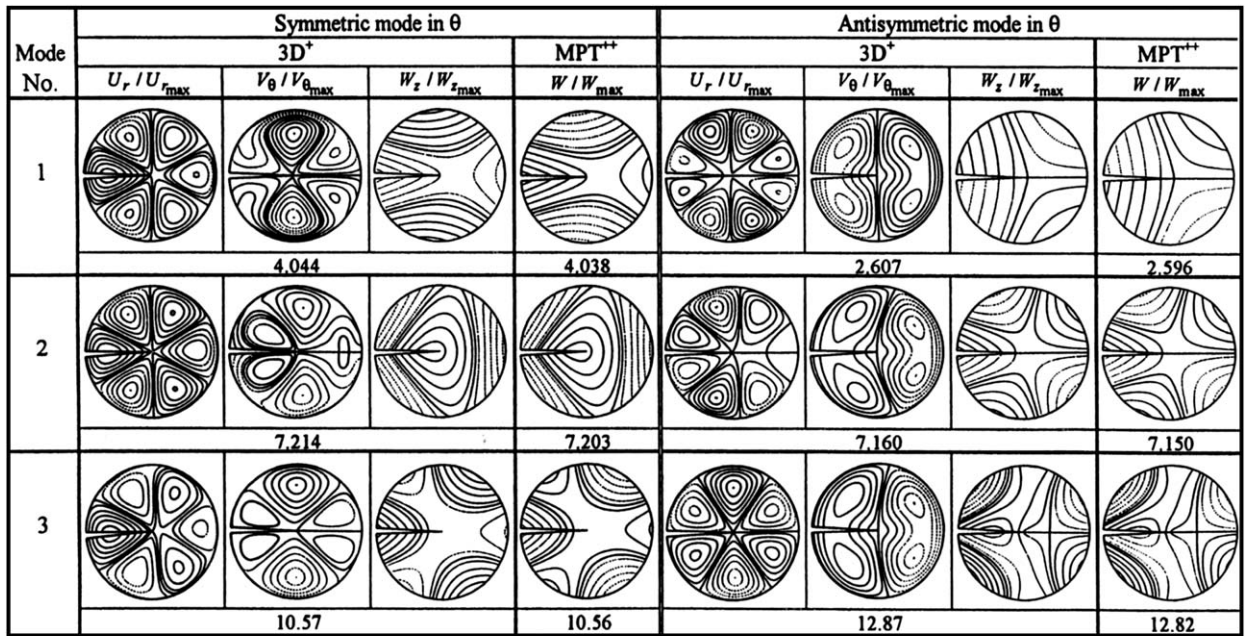
+ Present three-dimensional elasticity theory; ++ Present Mindlin plate theory (κ^2 = 5/6)

Fig. 6. Normalized displacement contours for a completely free thick sectorial plate (α=355°, c/a=0, a/h=5), results compared to a thick sectorial Mindlin plate [21,32].

respectively. For a thick cantilevered cylinders having h/a=2, the maximum reduction due to the crack is seen in Table 14 to be 34.1 percent in the second symmetric mode. For cracked cantilevered slender rods (h/a=6 and 10), reductions in $\omega a^2 \sqrt{\rho h/D}$ values of the symmetric modes are negligible, whereas a radial crack decreases the $\omega a^2 \sqrt{\rho h/D}$ values of the anti-symmetric modes by 3.8, 18.0, and 8.9 percent for h/a=6 and by 1.8, 21.9, and 5.3 percent for h/a=10.

Shown in Fig. 6 are normalized displacement contours for a thick (a/h=5) sectorial plate (c/a=0) with a notch angle of 5°. These contour plots are normalized at the middle surface of the sectorial plate with respect to the maximum in-plane and transverse displacement components (i.e., $-1 \le U_r/U_{r_{max}} \le 1$, $-1 \le V_\theta/V_{\theta_{max}} \le 1$, and $-1 \le W_z/W_{z_{max}} \le 1$, where the negative $U_r/U_{r_{max}}$, $V_\theta/V_{\theta_{max}}$, and $W_z/W_{z_{max}}$ are depicted as dashed contour lines in Fig. 6, and non-dimensional frequencies shown correspond to the data listed in Tables 10 and 11). Nodal patterns of each mode are shown in Fig. 6 as darker contour lines of
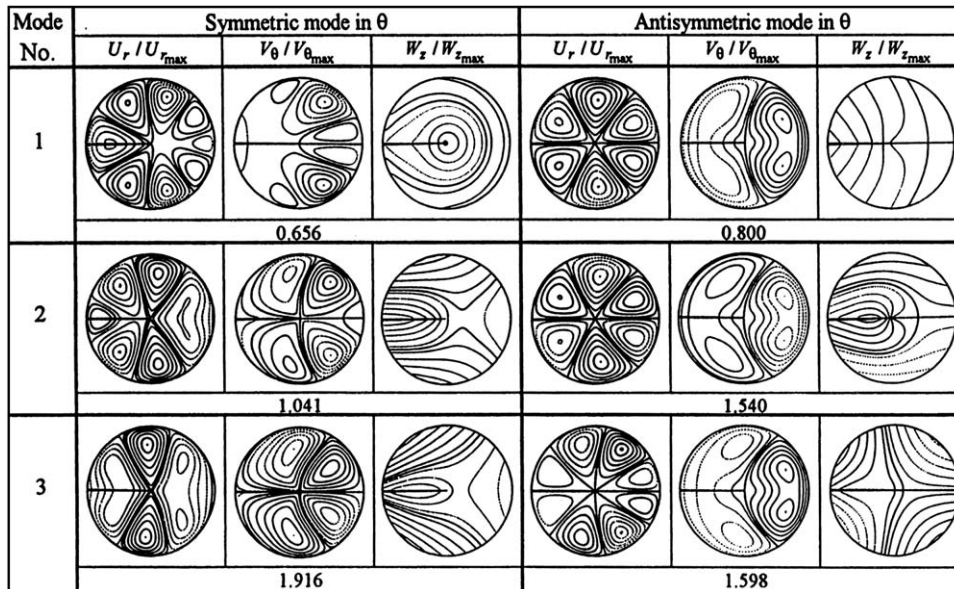
Mode No.	Symmetric mode in θ			Antisymmetric mode in θ		
	$U_r/U_{r_{max}}$	$V_\theta/V_{\theta_{max}}$	$W_z/W_{z_{max}}$	$U_r/U_{r_{max}}$	$V_\theta/V_{\theta_{max}}$	$W_z/W_{z_{max}}$
1						
		0.656			0.800	
2						
		1.041			1.540	
3						
		1.916			1.598	

Fig. 7. Normalized displacement contours for a completely free cylinder having a deep radial crack (α=359° c/a=0, h/a=2).

zero displacements during vibratory motion. For $U_r/U_{r_{max}}$ and $W_z/W_{z_{max}}$ contours, a horizontal nodal line passes through the terminus edge of the notch in the anti-symmetric modes. In contrast, for $V_\theta/V_{\theta_{max}}$ contours, that nodal line passes through the terminus edge of the notch in the symmetric modes. It is also seen in Fig. 6 that a sharp radial notch causes radial nodal lines extending from the terminus edge of the notch to the circumferential edge in the first anti-symmetric mode of the normalized transverse displacement contours ($W_z/W_{z_{max}}$). More specifically, it can be seen in Fig. 6 that the influence on the ($W_z/W_{z_{max}}$) contours of 3-D in-plane ($r^{\lambda-1}$-type) stress singularities and transverse ($r^{\bar{\lambda}}$-type singularity) stress singularities along the V-notch terminus edge of a thick (a/h=5) sectorial plate (c/a=0) with a notch angle of 5° have been compared to the influence on the ($W_z/W_{z_{max}}$) contours of the order of singularities for bending moments ($r^{\lambda-1}$-type singularity) and shear forces ($r^{\bar{\lambda}}$-type singularity) at the vertex of a thick sectorial Mindlin plate (where λ and $\bar{\lambda}$ are real or complex characteristic values for Mindlin plate [36,43] and 3-D elasticity-based [34] theories). The ($W_z/W_{z_{max}}$) contours predicted using the present 3-D elasticity theory are seen in Fig. 6 to be in favorable agreement with those predicted using Mindlin plate theory [36,43]. It has been also shown in Fig. 6 that the 3-D frequency solutions are in close agreement, as slightly higher upper bounds on the exact solution, compared with frequency results obtained by the Mindlin plate theory.

In Fig. 7, additional normalized displacement contours are plotted for a completely free cylinder having a notch angle of 1°, c/a=0 (idealizing a sharp, deep radial crack), and h/a=2. These contour plots are normalized at the top surface of the cracked cylinder with respect to the maximum in-plane and transverse displacement components and non-dimensional frequencies shown correspond to the data listed in Table 13. In the first and second symmetric mode of $W_z/W_{z_{max}}$ contours, the sharp curvature and distortion of the nodal lines is quite apparent due to the notch effect, more so for the cracked cylinder (Fig. 7) than the notched thick circular plate (Fig. 6). Interestingly, the radial nodal lines in the first anti-symmetric mode of $W_z/W_{z_{max}}$ contours shift away from the terminus edge of the notch. Comparing the normalized displacement contours and nodal patterns plotted in Figs. 6 and 7, it can be generally induced that the analogous classical Chaldni-type laboratory circular configuration vibration nodal pattern observations and findings [1] are predicted herein, for a notched or cracked thick sectorial plate (a/h=5) or cylinder solid (h/a=2), as significantly shifted by the singular stresses existing at the re-entrant terminus edge of the notch or crack.

6. Concluding remarks and further studies

In this work, it has been demonstrated that accurate non-dimensional frequencies and normalized displacement contours of V-notched cylindrical elastic solids can be predicted using a 3-D elasticity-based, reduced-order, weak formulation, variational Ritz procedure. No simplifying kinematic assumptions have been made on the strain distribution through the thickness of the elastic bodies, as typically used in rod, beam, plate and shell theories. The 3-D elasticity-based dynamical energies in the procedure incorporate for the in-plane and transverse displacement fields admissible hybrid trial functions of mathematically complete, algebraic–trigonometric polynomials in conjunction with admissible edge functions [34], which account for the tri-axial stress singularities occurring at the terminus edge/corner of a V-notch or a sharp radial crack. Depending on the boundary or face conditions existing, one must derive the alternate admissible forms of the

algebraic–trigonometric polynomials and edge functions used. The efficacy of the 3-D edge functions has been substantiated through an extensive convergence study of non-dimensional frequencies. It was seen that the edge functions accelerate the convergence rate of solutions.

The numerical results presented herein demonstrate the correctness and accuracy of the 3-D Ritz procedure utilized in this work. This is further substantiated by extensive convergence studies carried out for non-dimensional frequency parameters $\omega a^2 \sqrt{\rho h/D}$ used in this work. Extensive amount of non-dimensional frequency $\omega a^2 \sqrt{\rho h/D}$ data presented clearly indicates the influence of the edge functions on the upper-bound convergence of frequency solutions.

Detailed frequency data has been provided herein for completely free V-notched plates and for completely free and cantilevered cracked solid rods and cylinders using 3-D theory of elasticity. This provides the data which can be utilized to derive some fundamental understanding regarding the effect of stresses on the V-notched cylinders and thick circular plates used in industry applications for mechanical and structural systems. Detailed numerical tables of $\omega a^2 \sqrt{\rho h/D}$ (accurate up to four significant figures) for notched thick plates and cylinders have been presented for a wide range of notch depths c/a, vertex angles α, plate thickness ratios (a/h) and cylindrical height ratios (h/a). The frequency variation with notch depth was considerable, as expected, with larger variation in higher ranges of α, and smaller variation in lower ranges of α. The results have been compared with those obtained by Mindlin plate theory [36,43] and the classical thin plate theory [33]. Specifically, the influence of 3-D in-plane ($r^{\lambda-1}$-type) stress singularities and transverse ($r^{\bar{\lambda}}$-type singularity) stress singularities along the V-notch terminus edge of elastic solids have been compared to the influence of the order of singularities for bending moments ($r^{\lambda-1}$-type singularity) and shear forces ($r^{\bar{\lambda}}$-type singularity) at the vertex of Mindlin sectorial plate (where λ and $\bar{\lambda}$ are real or complex characteristic values for Mindlin plate [36,43], and 3-D elasticity-based [34] theories). It has been observed that Mindlin plate theory and 3-D theory of elasticity present significantly lower upper bounds on the exact solutions compared to the upper bound frequency predicted using classical thin plate theory [33].
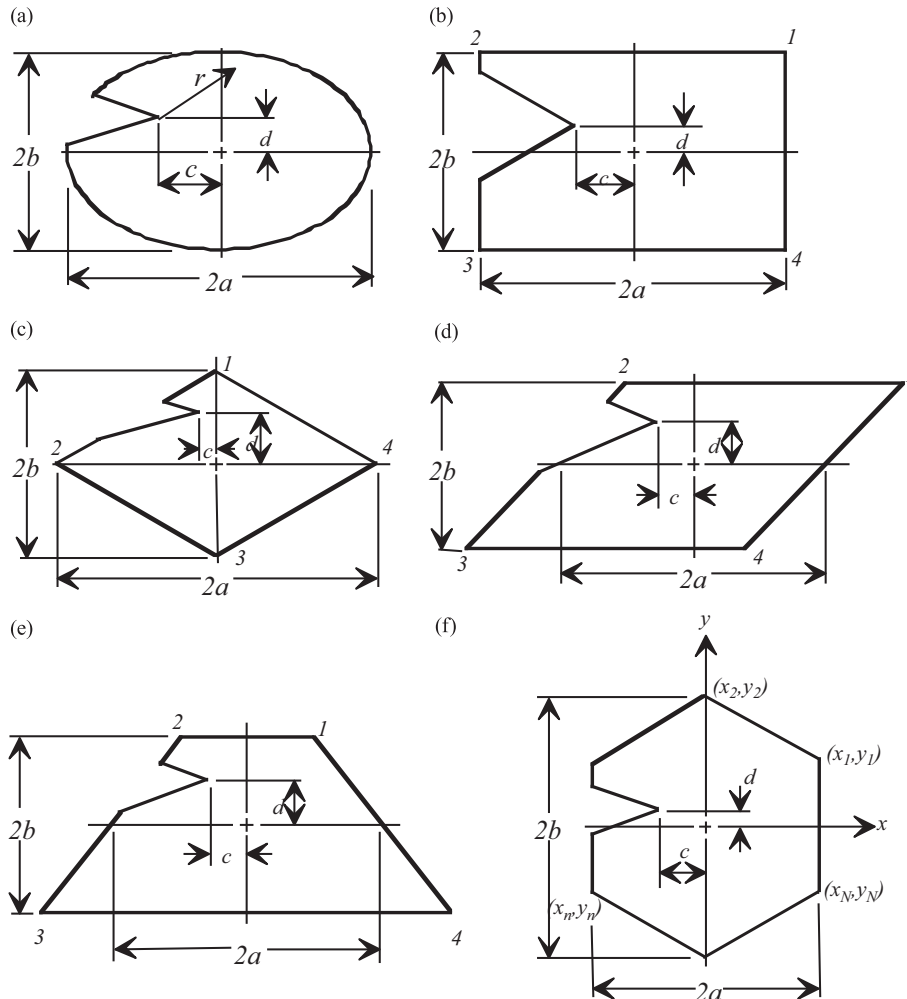

Fig. A1. Arbitrarily shaped elastic solids having a V-notch or sharp radial crack: (a) elliptical, (b) rectangular, (c) rhombus, (d) parallelogram, (e) trapezoid, and (f) N-sided polygon.

It has been also concluded that the 3-D frequency solutions are slightly higher upper bounds on the exact solution compared with the upper bound frequency results obtained by the Mindlin plate theory.

In reality, for $\alpha > 180°$, highly localized stresses at the vertex/terminus of sharp notches or cracks may become detrimental in connection with vibration, by constituting an origin for crack propagation during fatigue and a source of stress intensity at fracture. Some fundamental understanding of the effect of these localized stresses on V-notched circular plate and cylinder dynamics can be obtained through examination of the frequency data and characteristic modal shapes offered herein. What is discerned from these results is that the present method is an effective one for modeling the unbounded vibratory stresses, which exist at the vertex/terminus of cylindrical elastic bodies. Most of all very accurate vibration data have been offered in this paper for comparison with future data obtained by other investigators. The message the authors have attempted to convey is that investigators using continuum-based and discrete element-based formulations will have difficulty in obtaining accurate results unless they explicitly consider in the assumed displacements or stress fields the stress singularities at the re-entrant corner/edge.

In this paper a study has been restricted to analyzing the free vibration of completely free and cantilevered cylindrical elastic solids having V-notches. The accurate vibration data presented for 3-D elastic V-notched solids serves as benchmark values for comparisons with the data obtained by experiments and other theoretical approaches. However, the frequency solutions for the six representative elastic bodies shown in Figs. A1(a)–(f) can be easily obtained by changing the values of $r(\theta)$ (see Appendix A) in the integral of energy functional. The additional formulations in Appendix A generalize the present analysis for future follow-on extensions used by other investigators to examine 3-D vibrations of arbitrarily shaped V-notched thick plates [50,51] and generally shaped V-notched elastic bodies. Also, the present research can be also extended to investigate the vibration problems of elastic solids having V-notches with the other combinations of radial boundary conditions. For this study, the Mindlin corner functions and 3-D edge functions have been provided in McGee et al. [36] and McGee and Kim [34], respectively. Additional computational studies are required to fully address such follow-on problems proposed here.

Specifically, the present research can be extended to address computational issues related to singular solutions of 2- and 3-D boundary-value problems using finite element methods coupled with acceptable sub-domain approaches [52,53], such as Ritz-type super-elements (involving the elastic bodies herein) and boundary elements. From current engineering practices, it has been found that the existence of stress singularities within the domain of various boundary-value problems of applied mechanics deteriorates the accuracy of solutions obtained from quasi-uniform finite element meshes. In the singular problems, gradients of the solution become infinite with abrupt local variations near the sharp corner/edge of the V-notch. An accurate prediction of these gradient variations may be obtained efficiently by using singular Ritz super-elements akin to the elasticity-based V-notched cylindrical bodies examined herein. These singular super-elements may be implemented as substructures or sub-models of specified sub-domains defined by various geometric, load, and material parameters. Finite element analysis of singular mechanics problems will be more efficiently parameterized and customized, when analysts will develop a primary finite element analysis domain in conjunction with sub-domain analyses via singular Ritz super-elements comprised of the elasticity-based mechanics of V-notched cylindrical bodies.

Appendix A. Domain descriptions of arbitrary shapes of elastic bodies having a V-notch or sharp radial crack

The expressions of $r(\theta)$ used to perform the numerical volumetric integrations in Eqs. (9)–(11) along an arbitrarily shaped circumferential edge (Fig. 1), represented as an elliptical, rectangular parallelepiped, rhombic, parallelogramic, trapezoidal, or N-sided polyhedron shapes.

(1) *Elliptical* V-*notched solid* (Fig. A1(a)):

$$r(\theta) = \frac{\delta_2 + \sqrt{\delta_2^2 - \delta_1 \delta_3}}{\delta_1} (-\pi \le \theta \le \pi),$$

(A.1)

where

$$\delta_1 = \frac{\cos^2 \theta}{a^2} + \frac{\sin^2 \theta}{b^2},$$

$$\delta_2 = \frac{c \cos \theta}{a^2} + \frac{d \sin \theta}{b^2},$$

$$\delta_3 = \frac{c^2}{a^2} + \frac{d^2}{b^2} - 1.$$

(2) *Rectangular parallelepiped* V-*notched solid* (Fig. A1(b)):

$$r(\theta) = \frac{b - d}{\sin \theta} \ (\theta_1 \le \theta \le \theta_2),$$

(A.2a)

$$r(\theta) = -\frac{a - c}{\cos \theta} \ (\theta_2 \le \theta \le \theta_3),$$

(A.2b)

$$r(\theta) = -\frac{b+d}{\sin\theta} \ (\theta_3 \le \theta \le \theta_4), \tag{A.2c}$$

$$r(\theta) = \frac{a+c}{\cos\theta} \ (\theta_4 \le \theta \le \theta_1), \tag{A.2d}$$

where

$$\theta_1 = \tan^{-1}\left(\frac{b-d}{a+c}\right), \quad \theta_2 = -\tan^{-1}\left(\frac{b-d}{a-c}\right),$$

$$\theta_3 = \tan^{-1}\left(\frac{b+d}{a-c}\right), \quad \theta_4 = -\tan^{-1}\left(\frac{b+d}{a+c}\right),$$

(3) *Rhombic* V-*notched solid* (Fig. A1(c)):

$$r(\theta) = \frac{b-d-bc/a}{\sin\theta - (b\cos\theta)/a} \ (\theta_1 \le \theta \le \theta_2), \tag{A.3a}$$

$$r(\theta) = \frac{b+d-bc/a}{\sin\theta + (b\cos\theta)/a} \ (\theta_2 \le \theta \le \theta_3), \tag{A.3b}$$

$$r(\theta) = \frac{b+d+bc/a}{\sin\theta - (b\cos\theta)/a} \ (\theta_3 \le \theta \le \theta_4), \tag{A.3c}$$

$$r(\theta) = \frac{b-d+bc/a}{\sin\theta + (b\cos\theta)/a} \ (\theta_4 \le \theta \le \theta_1), \tag{A.3d}$$

where

$$\theta_1 = \tan^{-1}\left(\frac{b-d}{c}\right), \quad \theta_2 = -\tan^{-1}\left(\frac{d}{a-c}\right),$$

$$\theta_3 = -\tan^{-1}\left(\frac{b+d}{c}\right), \quad \theta_4 = -\tan^{-1}\left(\frac{d}{a+c}\right),$$

(4) *Parallelogram-shaped* V-*notched solid* (Fig. A1(d)):

$$r(\theta) = \frac{b-d}{\sin\theta} \ (\theta_1 \le \theta \le \theta_2), \tag{A.4a}$$

$$r(\theta) = \frac{a-c-d/s}{(\sin\theta)/s - \cos\theta} \ (\theta_2 \le \theta \le \theta_3), \tag{A.4b}$$

$$r(\theta) = -\frac{b+d}{\sin\theta} \ (\theta_3 \le \theta \le \theta_4), \tag{A.4c}$$

$$r(\theta) = -\frac{a+c+d/s}{(\sin\theta)/s - \cos\theta} \ (\theta_4 \le \theta \le \theta_1), \tag{A.4d}$$

where

$$\theta_1 = \tan^{-1}\left(\frac{b-d}{a+c+b/s}\right), \quad \theta_2 = -\tan^{-1}\left(\frac{b-d}{a-c-b/s}\right),$$

$$\theta_3 = \tan^{-1}\left(\frac{b+d}{a-c+b/s}\right), \quad \theta_4 = -\tan^{-1}\left(\frac{b+d}{a+c-b/s}\right),$$

and

$$s = \text{slope of the sides of parallelogram.}$$

(5) *Trapezoidal-shaped* V-*notched solid* (Fig. A1(e)):

$$r(\theta) = \frac{b-d}{\sin\theta} \ (\theta_1 \le \theta \le \theta_2), \tag{A.5a}$$

$$r(\theta) = \frac{a-c-d/s_2}{(\sin\theta)/s_2 - \cos\theta} \ (\theta_2 \le \theta \le \theta_3), \tag{A.5b}$$

$$r(\theta) = -\frac{b+d}{\sin\theta} \ (\theta_3 \le \theta \le \theta_4), \tag{A.5c}$$

$$r(\theta) = \frac{a+c-d/s_1}{(\sin\theta)/s_1 + \cos\theta} \ (\theta_4 \le \theta \le \theta_1), \tag{A.5d}$$

where

$$\theta_1 = \tan^{-1}\left(\frac{b-d}{a+c-b/s_1}\right), \quad \theta_2 = -\tan^{-1}\left(\frac{b-d}{a-c-b/s_2}\right),$$

$$\theta_3 = \tan^{-1}\left(\frac{b+d}{a-c+b/s_2}\right), \quad \theta_4 = -\tan^{-1}\left(\frac{b+d}{a+c+b/s_1}\right),$$

and

$$s_1 = \text{slope of the right side of trapezoid},$$

$$s_2 = \text{slope of the left side of trapezoid}.$$

(6) *N-sided polyhedron* V-*notched solid* (Fig. A1(f)):

$$r(\theta) = \frac{|y_n - x_n \tan\eta_n|}{\sin\theta - \tan\eta_n \cos\theta}(-\pi \le \theta \le \pi), \tag{A.6a}$$

where *n*=1,2,…,*N* (*N*=number of sides). The above equation can be applied to all range of θ for *N*-sided polygon except following cases:

$$r(\theta) = -\frac{a-c}{\cos\theta}(\theta_{N/2} \le \theta \le \theta_{N/2+1}), \tag{A.6b}$$

$$r(\theta) = \frac{a+c}{\cos\theta}(\theta_N \le \theta \le \theta_1). \tag{A.6c}$$

In Eq. (6a),

$$\begin{cases} \eta_1 = \beta + \dfrac{\pi}{2} \\ \eta_n = \eta_{n-1} + \beta \end{cases} (n = 2,3,\dots,N),$$

$$\begin{cases} x_1 = a+c \\ x_n = x_{n-1} + L\cos\eta_{n-1} \end{cases} (n = 2,3,\dots,N),$$

$$\begin{cases} y_1 = \dfrac{L}{2} - d \\ y_n = y_{n-1} + L\sin\eta_{n-1} \end{cases} (n = 2,3,\dots,N),$$

in which

$$\beta = \frac{2\pi}{N},$$

$$L = 2a\tan\frac{\beta}{2}.$$

References

[1] A.W. Leissa, *Vibration of Plates*, *Vibration of Shells*, US Government Printing Office (Reprinted by The Acoustical Society of America, 1993).
[2] L. Pochhamer, Uber die Fortpflanzungsgeschwindigkeiten Kleiner Schwingungen in Einem Unbegrenzten Isotropen Kreiscylinder, *Zeitschrift fur Reine und Angewandte Mathematik* 81 (1876) 324–336.
[3] C. Chree, The equations of an isotropic elastic solid in polar and cylindrical coordinates, their solutions and applications, *Transactions of the Cambridge Philosophical Society* 14 (1889) 250–309.
[4] J.E. Greenspon, Flexural vibrations of a thick-walled circular cylinder according to the exact theory of elasticity, *Journal of Aerospace Sciences* 27 (1957) 1365–1373.
[5] D.C. Gazis, Three-dimensional investigation of the propagation of waves in hollow circular cylinder, *Journal of the Acoustical Society of America* 31 (1959) 568–578.
[6] A.E. Armenakas, Propagation of harmonic waves in composite circular cylindrical shells—I: theoretical investigations, *AIAA Journal* 5 (1967) 740–744.
[7] G. Pickett, Flexural vibration of unrestrained cylinders and disks, *Journal of Applied Physics* 16 (1945) 820–831.
[8] S.N. Rasband, Resonant vibrations of free cylinders and disks, *Journal of the Acoustical Society of America* 57 (4) (1975) 899–905.
[9] H.D. McNiven, D.C. Perry, Axially symmetric waves in finite, elastic rods, *Journal of the Acoustical Society of America* 34 (4) (1962) 433–437.

[10] H.D. McNiven, A.H. Shah, J.L. Sackman, Axially symmetric waves in hollow, elastic rod—part 1, *Journal of the Acoustical Society of America* 40 (1966) 784–791.
[11] G.W. McMahon, Experimental vibrations of beams, exact versus approximate solutions, *Journal of the Acoustical Society of America* 36 (1) (1964) 85–92.
[12] G.W. McMahon, Finite-difference analysis of the vibrations of solid cylinders, *Journal of the Acoustical Society of America* 48 (1) (1970) 307–312.
[13] W.E. Tefft, Numerical solutions of the frequency equations for the flexural vibrations of cylindrical rods, *Journal of Research of the National Bureau of Standards* 64 (B) (1969) 237–242.
[14] M. Rumerman, S. Raynor, Natural frequencies of finite circular cylinders in axially symmetric longitudinal vibration, *Journal of Sound and Vibration* 15 (4) (1971) 529–543.
[15] H.C. Wang, P.K. Banerjee, Axisymmetric free-vibration problems boundary element method, *ASME Journal of Applied Mechanics* 55 (1988) 437–442.
[16] J.R. Hutchinson, Transverse vibrations of beams, exact versus approximate solutions, *ASME Journal of Applied Mechanics* 48 (1981) 923–928.
[17] G.M. Gladwell, U.C. Tahbildar, Finite element analysis of axisymmetric vibrations of cylinders, *Journal of Sound and Vibration* 22 (1972) 143–157.
[18] G.M. Gladwell, D.K. Vijay, Natural frequencies of free finite length circular cylinders, *Journal of Sound and Vibration* 42 (1975) 387–397.
[19] J.R. Hutchinson, Axisymmetric vibrations of a free finite length rod, *Journal of the Acoustical Society of America* 51 (1972) 233–240.
[20] J.R. Hutchinson, Vibrations of solid cylinders, *ASME Journal of Applied Mechanics* 47 (1980) 901–907.
[21] J.R. Hutchinson, S.A. El-Azhari, Vibrations of free hollow circular cylinders, *ASME Journal of Applied Mechanics* 53 (1986) 641–646.
[22] R.K. Singal, K. Williams, A theoretical and experimental study of vibrations of thick circular cylindrical shells and rings, *ASME Journal of Vibration, Acoustics, Stress, and Reliability in Design* 110 (1988) 533–537.
[23] A.W. Leissa, J. So, Comparisons of vibration frequencies for rods and beams from one-dimensional and three-dimensional analyses, *Journal of the Acoustical Society of America* 98 (4) (1995) 2122–2135.
[24] A.W. Leissa, J. So, Accurate vibration frequencies of circular cylinders from three-dimensional analysis, *Journal of the Acoustical Society of America* 98 (4) (1995) 2136–2141.
[25] J. So, A.W. Leissa, Free vibrations of thick hollow circular cylinders from three-dimensional analysis, *ASME Journal of Vibration and Acoustics* 119 (1997) 89–95.
[26] K.M. Liew, K.C. Hung, Three-dimensional vibratory characteristics of solid cylinders and some remarks of simplified beam theories, *International Journal of Solids and Structures* 32 (1995) 3499–3513.
[27] K.M. Liew, K.C. Hung, M.K. Lim, Vibration of stress free hollow cylinders of arbitrary cross-section, *ASME Journal of Applied Mechanics* 62 (1995) 718–724.
[28] K.C. Hung, K.M. Liew, M.K. Lim, Free vibration of cantilevered cylinders: effects of cross-sections and cavities, *Acta Mechanica* 113 (1995) 37–52.
[29] H. Wang, K. Williams, Vibrational modes of thick cylinders of finite length, *Journal of Sound and Vibration* 191 (1996) 955–971.
[30] D. Zhou, Y.K. Cheung, S.H. Lo, F.T.K. Au, Three-dimensional vibration analysis of solid and hollow circular cylinders via Chebyshev–Ritz method, *Computer Methods in Applied Mechanics and Engineering* 192 (2003) 1575–1589.
[31] J.H. Lee, J. Kim, Analysis and measurement of sound transmission through a double-walled cylindrical shell, *Journal of Sound and Vibration* 251 (2002) 631–649.
[32] D.D. Ebenezer, K. Ravichandran, C. Padmanabhan, Forced vibrations of solid elastic cylinders, *Journal of Sound and Vibration* 282 (3–5) (2005) 991–1007.
[33] A.W. Leissa, O.G. McGee, C.S. Huang, Vibrations of circular plates having V-notches or sharp radial cracks, *Journal of Sound and Vibration* 161 (2) (1993) 227–239.
[34] O.G. McGee III, J.W. Kim, Sharp edge functions for three-dimensional elastic solids, *ASME Journal of Applied Mechanics* (2009), to appear.
[35] R.D. Mindlin, Influence of rotatory inertia and shear on flexural motions of isotropic, elastic plates, *ASME Journal of Applied Mechanics* 18 (1951) 31–38.
[36] O.G. McGee, J.W. Kim, A.W. Leissa, Sharp corners in Mindlin plate vibrations, *ASME Journal of Applied Mechanics* 72 (1) (2005) 1–9.
[37] G.C. Sih, M.L. Williams, J.L. Swedlow, *Three-Dimensional Stress Distribution Near a Sharp Crack in a Plate of Finite Thickness*, AMFL-TR-66-242, Air Force Materials Laboratory, Wright-Patterson Air Force Base, 1966.
[38] R.J. Hartranft, G.C. Sih, The use of eigenfunction expansions in the general solution of three-dimensional crack problems, *Journal of Mathematics and Mechanics* 19 (2) (1969) 123–138.
[39] E.S. Folias, On the three-dimensional theory of cracked plates, *ASME Journal of Applied Mechanics* 42 (1975) 663–674.
[40] W. Shaofu, Z. Xing, H. Qingzhi, Functional variable displacement method in analysis of singularity near the corner point in a three-dimensional cracked solid, *Engineering Fracture Mechanics* 31 (2) (1988) 191–200.
[41] I.Y. Shen, Vibration of a three-dimensional, finite linear, elastic solid containing cracks, *ASME Journal of Applied Mechanics* 62 (1995) 282–288.
[42] G.P. Tandon, R.Y. Kim, S.G. Warrier, B.S. Majumdar, Influence of free edge and corner singularities on interfacial normal strength: application in model unidirectional composites, *Composites Part B: Engineering* 30 (2) (1999) 115–134.
[43] O.G. McGee III, J.W. Kim, Vibrations of completely free arbitrarily-shaped Mindlin plates with V-notches and sharp radial cracks, *ASME Journal of Applied Mechanics* (2009) to appear.
[44] A.W. Leissa, O.G. McGee, C.S. Huang, Vibrations of sectorial plates having corner stress singularities, *ASME Journal of Applied Mechanics* 60 (1) (1993) 134–140.
[45] C.S. Huang, A.W. Leissa, O.G. McGee, Exact analytical solutions for the vibrations of sectorial plates with simply supported radial edges, *ASME Journal of Applied Mechanics* 60 (1993) 478–483.
[46] O.G. McGee, A.W. Leissa, C.S. Huang, J.W. Kim, Vibrations of circular plates with clamped V-notches or rigidly constrained radial cracks, *Journal of Sound and Vibration* 181 (2) (1995) 185–201.
[47] C.S. Huang, O.G. McGee, A.W. Leissa, Exact analytical solutions for free vibrations of thick sectorial plates with simply supported radial edges, *International Journal of Solids and Structures* 31 (11) (1994) 1609–1631.
[48] E. Reissner, The effects of transverse shear deformation on the bending of elastic plates, *ASME Journal of Applied Mechanics* 12 (1945) 69–77.
[49] M.R. Mofakhamia, H.H. Toudeshkya, S.H. Hashemib, Finite cylinder vibrations with different end boundary conditions, *Journal of Sound and Vibration* 297 (2006) 293–314.
[50] D.H. Geiger, Irregular shaped plates with singularities, *ASCE Journal of Engineering Mechanics* 97 (5) (1971) 1533–1553.
[51] K. Nagaya, Direct method for the determination of eigen-frequencies of arbitrarily shaped plates, *Journal of Vibration, Acoustics, Stress and Reliability in Design* 105 (1) (1983) 132–136.
[52] P. Guruswamy, T.Y. Yang, A sector finite element for dynamic analysis of thick plates, *Journal of Sound and Vibration* 62 (4) (1979) 505–516.
[53] T.M. Hrudey, M.M. Hrabok, Singularity finite elements for plate bending, *ASCE Journal of Engineering Mechanics* 112 (7) (1986) 666–681.